Ad Hoc Networks 185 (2026) 104158

Contents lists available at ScienceDirect

Ad Hoc Networks

journal homepage: www.elsevier.com/locate/adhoc

qIoV: A quantum-driven approach for environmental monitoring and rapid response systems using internet of vehicles

Ankur Nahar [a,*], Koustav Kumar Mondal [b], Debasis Das [b,*], Rajkumar Buyya [c]

[a] Harish and Bina Shah School of AI & CS, Plaksha University, SAS Nagar, India
[b] Indian Institute of Technology Jodhpur, India
[c] Cloud Computing and Distributed Systems (CLOUDS) Lab, School of Computing and Information Systems, The University of Melbourne, Australia

ARTICLE INFO

Keywords:
Internet of vehicles
Quantum computing
Quantum mesh network fabric
Rapid response systems
Variational quantum classifier

ABSTRACT

This paper addresses the critical demand for advanced rapid response mechanisms in managing a wide array of environmental hazards, including urban pipeline leaks, industrial gas discharges, methane emissions from landfills, chlorine leaks from water treatment plants, and residential carbon monoxide releases. Conventional sensing and alert systems often struggle with the timely analysis of high-dimensional sensor data and suffer delays as data volume increases. We propose a novel framework, *qIoV*, which integrates quantum computing with the Internet of Vehicles (IoVs) to leverage the computational efficiency, parallelism, and entanglement properties inherent in quantum mechanics. The qIoV framework utilizes vehicular-mounted environmental sensors for highly accurate air quality assessments, where quantum principles enhance both sensitivity and precision. A core innovation is the Quantum Mesh Network Fabric (QMF), which dynamically adapts the quantum network topology to vehicular movement, maintaining quantum state integrity among environmental and vehicular disruptions, thereby ensuring robust data transmission. Furthermore, we implement a variational quantum classifier (VQC) with advanced entanglement techniques, significantly reducing latency in hazard alerts and facilitating rapid communication with emergency response teams and the public. Our experimental evaluations using the IBM OpenQASM 3 platform with a 127-qubit system achieved over 90% precision, recall, and F1-score in pair plot analysis, alongside an 83% increase in toxic gas detection speed compared to conventional methods. Theoretical analysis further substantiates the efficiency of quantum rotation, teleportation protocols, and the fidelity of quantum entanglement, highlighting the potential of quantum computing in environmental hazard management.

1. Introduction

Gas leaks in urban areas present significant hazards, with the absence of rapid response systems often exacerbating their impact. From 2010 to 2021, the United States experienced over 2600 gas pipeline leaks [1], while China's coal mining industry reported 3695 fatalities between 2001 and 2018 [2]. Additionally, 4901 oil and gas spills were recorded in the U.S. from 2010 to 2022, with Texas alone accounting for nearly 40% [3]. The Bhopal gas leak disaster in India, which resulted in thousands of deaths, emphasizes the need for efficient alert systems [4]. Recent regulatory efforts in the U.S. to address methane leaks further highlight the ongoing challenges [5]. Early warning systems play a crucial role in mitigating the impact of environmental disasters by facilitating rapid evacuations, timely medical aid, and swift emergency responses, especially during gas leaks [6]. While wireless sensor networks [7] and classical machine learning algorithms [8] remain more scalable on conventional hardware, they encounter exponential computational complexity with extremely high-dimensional data, such as multi-sensor inputs in industrial monitoring. In contrast, quantum machine learning (QML) leverages quantum parallelism, enabling more efficient handling of exponentially complex feature spaces. Notably, QML models, such as Variational Quantum Classifiers (VQC), achieve comparable accuracies with up to 50% fewer training samples and parameters, outperforming classical AI in specific high-dimensional problems [9]. Quantum systems, despite their susceptibility to environmental noise and associated error rates, can exploit the sensitivity to detect subtle environmental changes. This characteristic allows quantum algorithms to identify minute variations in environmental data, proving especially effective for detecting hazardous gas leaks beyond the capabilities of classical methods.

* Corresponding authors.
E-mail addresses: ankur.nahar@plaksha.edu.in (A. Nahar), mondal.4@iitj.ac.in (K.K. Mondal), debasis@iitj.ac.in (D. Das), rbuyya@unimelb.edu.au (R. Buyya).

https://doi.org/10.1016/j.adhoc.2026.104158
Received 21 November 2025; Received in revised form 18 January 2026; Accepted 27 January 2026
Available online 2 February 2026

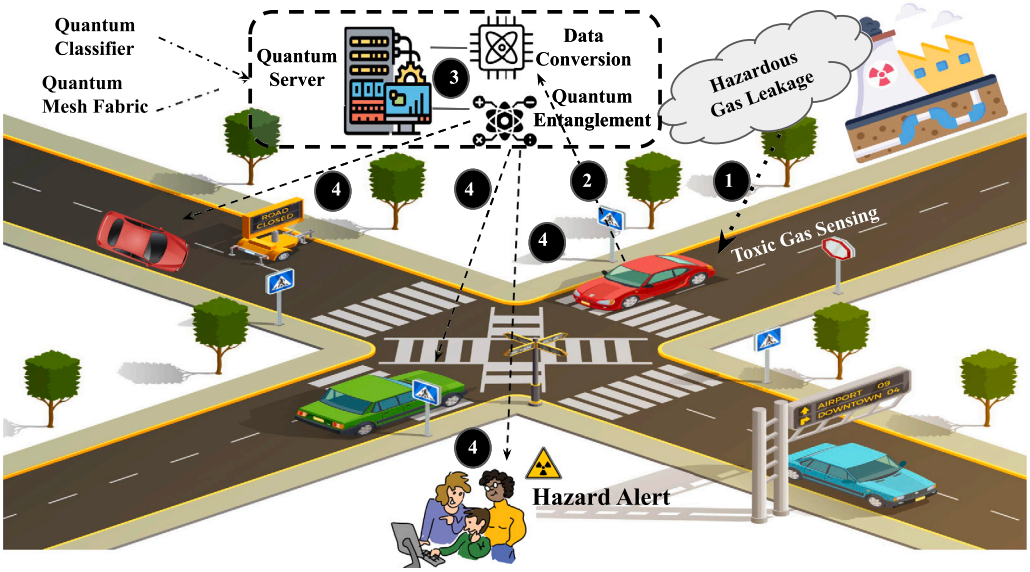

Fig. 1. qIoV: A quantum framework for toxic gas detection.

Our research addresses three primary challenges: converting classical sensor data into quantum formats, employing quantum classifiers for hazard detection, and leveraging quantum entanglement for efficient alert dissemination within vehicular networks. Given the ubiquity of vehicles in urban areas, they serve as mobile environmental monitoring units equipped with sensors (e.g., MQ2, MQ3, MQ5, MQ6, MQ7, MQ8, and MQ135), capable of collecting real-time data critical for hazard detection. These 'MQ' sensors are semiconductor gas detectors, each calibrated for specific gases — for instance, MQ2 responds to flammable gases and smoke, MQ7 is sensitive to carbon monoxide, and MQ135 targets carbon dioxide and other air pollutants. By deploying a spectrum of such sensors, the system can detect a wide range of toxic gas leaks. However, the volume and complexity of this data pose challenges for traditional processing methods [10]. The proposed framework, shown in Fig. 1, integrates a quantum classifier, quantum mesh fabric (QMF), and quantum server for sustainable environmental safety. In Step 1, vehicle-mounted sensors detect toxic gasses from sources such as industrial sites or pipelines, capturing high-resolution data. Step 2 converts this data into a quantum-compatible format for processing by quantum algorithms. Step 3 focuses on the QMF and Quantum Server, where the QMF manages dynamic quantum state entanglement across the network, ensuring reliable communication, while the Quantum Server processes the data using quantum algorithms. Step 4 generates actionable intelligence utilizing the QMF to distribute hazard alerts across the network leveraging quantum entanglement faster information transmission.

1.1. Motivation

The recurrence of disastrous environmental emergencies and toxic gas outbreaks globally underscores the urgency of this research. AI-based control systems, while prevalent in industrial environments, frequently suffer from high false alarm rates, exceeding 30% due to sensor noise and machinery-induced interference. Reduced sensor sensitivity and diminished human oversight during nighttime hinder the effective detection, prediction, and warning of toxic hazards [11]. Notable examples are the Bhopal gas tragedy in India [12], Philadelphia refinery explosion, 2019 [13] and frequent toxic gas incidents in China highlight the increased risks during periods of reduced human activity, emphasizing the need for continuous, 24-h monitoring systems.

Why chose vehicles? Vehicles, due to their ubiquity and mobility, offer extensive coverage and continuous presence in urban areas, making them ideal for large-scale, high-resolution environmental monitoring. Equipped with sensors, vehicles enable constant monitoring across diverse geographic regions, surpassing the limited spatial range of fixed sensors confined to specific locations. This mobility allows vehicles to detect gas leaks beyond the reach of stationary systems, such as along transport routes or near temporary industrial sites. Additionally, their movement enables the detection of trace gas concentrations that may be dispersed over distances, detections that stationary systems often miss due to fixed positioning and signal attenuation. For instance, a mobile vehicle can identify a diffuse methane leak across a wide area, while fixed sensors may only register high concentrations within their immediate vicinity. Thus, vehicles significantly enhance spatial and temporal resolution, offering a more adaptive and effective solution.

The role of technology? Quantum computing offers transformative data processing capabilities using quantum bits (qubits), which can exist in multiple states simultaneously (superposition) and be entangled, creating complex probabilistic relationships. This enables parallel processing, allowing quantum systems to analyze large datasets and execute algorithms far more rapidly than traditional computing. In vehicular networks, this quantum advantage facilitates efficient encoding, processing, and interpretation of environmental data collected by sensors, enabling rapid in-situ analysis and reducing the latency of hazard detection compared to centralized systems. Furthermore, vehicular systems can dynamically adapt their QMF topology based on movement, maintaining stable entanglement and data transmission even as vehicles change location. This adaptability overcomes the limitations of fixed networks, which often suffer from signal degradation and data loss due to shifting conditions.

1.2. Contributions

qIoV framework introduces an entangled quantum feature mapping in the context of vehicular networks utilizing multipartite entanglement to encode sensor data. qIoV incorporates quantum feature maps for data representation and utilizes entanglement directly tied to hazard information encoding and teleportation-based alert dissemination, which has not been explored before. Furthermore, our integration of the Quantum Fourier Transform (QFT) for embedding environmental data and a fidelity-driven VQC optimization mechanism is a novel combination. The key contributions of this paper are as follows:

1. Quantum Encoding Scheme: We propose a quantum encoding scheme that aligns multi-dimensional vehicular sensor data with quantum states, optimizing rotation angles ($\mathbf{R}_\theta$) based on specific gas sensor readings to enhance toxic gas detection accuracy.
2. Multipartite Entanglement Model: We introduce a multipartite entanglement model for vehicular networks using Quantum Entangled Feature Maps. This involves systematic qubit entanglement across vehicles through controlled-Z (CZ) and controlled-X (CX) gates, establishing correlations that reflect the interconnected data patterns from vehicular sensors.
3. Scalable Entanglement Structure: The framework structures entanglement into scalable layers, accommodating dynamic vehicular networks by adjusting entanglement patterns to match varying network size and complexity.
4. Quantum Circuit Optimization: The framework implements adaptive quantum circuit optimization, guided by error syndromes and decoherence patterns detected through stabilizer codes. This approach fine-tunes quantum gate parameters, ensuring robust error correction and maintaining high fidelity in quantum state transmission across vehicular networks.

These contributions, particularly the entangled feature mapping and layered quantum entanglement strategy, represent a novel paradigm not present in previous Internet of Vehicles or environmental sensing studies. Our framework fuses advanced quantum communication (teleportation via pre-shared entanglement) with quantum machine learning for IoV-based environmental hazard detection. The structure of the rest of the article is as follows: Section 2 reviews the existing literature on quantum computing in computational contexts. Section 3 outlines the problem definition, while Section 4 details the system overview and architectural design. Section 5 introduces the proposed *qIoV* framework. Section 6 presents the simulation results and testing, and finally, Section 7 concludes the paper.

2. Related work

This section focuses on related works that advance our understanding of quantum machine learning, its applications in transportation, and emerging quantum frameworks and protocols. Additionally, it examines the current state of quantum technology, including its challenges and innovations, to establish a foundational context for our research.

2.1. Quantum foundations and data networks

The convergence of machine learning algorithms and quantum computing offers a transformative approach for processing high-dimensional, complex datasets. A research in [14] demonstrated the potential of qubits in enhancing computational efficiency, focusing on hybrid quantum–classical systems that harness quantum advantages. Despite improved computational capabilities, scalability and inherent noise remain significant limitations. Further advancements in [15], demonstrated that modern quantum hardware now supports configurations with thousands of qubits, significantly enhancing computational speed and efficiency. However, ongoing challenges, including system instability, resource constraints, communication barriers, and security vulnerabilities, remain critical obstacles. Quantum machine learning's complexities are also examined in [16,17], highlighting the field's evolution amid hardware and algorithmic challenges. A hybrid quantum–classical framework proposed in [18] addressed network resource optimization using quantum annealing for integer programming problems, but struggled with continuous optimization challenges. Concurrently, [19] noted a shift from hardware to software innovations, accelerating advancements in quantum image processing, machine learning, and sensory technologies.

To tackle quantum networking complexities, [20] analyzed entanglement swapping and optimization within non-associative quantum repeater chains, while [21] introduced a distributed computing model for quantum data networks (QDNs) to mitigate scalability issues by pooling computational power from multiple quantum-enabled devices. Nevertheless, QDNs face challenges such as the no-cloning theorem, quantum channel loss, stochastic entanglement link establishment, rapid decoherence, and single-photon detection inefficiencies. Research into QDN transport layer protocols in [22] emphasized efficient qubit exchange across quantum computers, highlighting the necessity of dynamic quantum memory management due to its scarcity. The QuantumFlow framework introduced in [23] proposed a method for representing data as unitary matrices, enabling input encoding with fewer qubits and reducing computational costs; however, practical scalability remains limited by current hardware constraints, such as qubit availability and error rates. Further, [24] investigated the execution of quantum algorithms beyond current qubit capacities by utilizing the quantum Internet to distribute tasks across multiple quantum processing units (QPUs), contingent on developing a robust quantum Internet infrastructure.

2.2. Emerging quantum frameworks and protocols

Focusing on sector-specific applications, [25] examined quantum computing's potential in transportation modeling but faced difficulties in adapting classical algorithms to quantum paradigms due to the unitary and reversible nature of quantum operations. Similarly, [26] proposed an edge server placement strategy utilizing binary and quantum encoding, but encountered computational intensity challenges. In [27], quantum approximate optimization algorithms were applied to vehicle routing, revealing challenges linked to the early stage of quantum devices. Innovative frameworks by [28,29] integrated federated learning with quantum teleportation and combined non-fungible tokens (NFTs) with quantum algorithms for wireless communication and IoVs, respectively. However, both faced difficulties in managing the complexity of quantum neural networks and IoVs scalability. [30] introduced an asynchronous entanglement distribution protocol for quantum networks, though it required intricate coordination among network nodes, adding complexity compared to synchronous alternatives. Additional researchers, in [10,31], discussed hybrid quantum–classical methods for sensor placement and vehicle routing, underscoring technological limitations. In other applications, [32] applied quantum machine learning to asteroid classification, encountering challenges with quantum processors and data management. Concurrently, [33,34] addressed database query processing and IoVs resource management, focusing on scalability, reliability, and the constraints of current quantum computing capabilities. [35] investigated reconfigurable intelligent surfaces (RISs) within a quantum computing-based algorithm for RIS selection to optimize qubit transmission in vehicular networks. While this method improved communication reliability, it required advanced control algorithms to manage RISs in dynamic environments. For ease of understanding Table 1 provide a summary of quantum computing applications in networks.

Our approach differentiates itself from existing research by employing entangled quantum feature mapping for intricate data encoding, a technique not previously explored, which allows for a more accurate representation of sensor data in quantum states. Additionally, the use of a parameterized ansatz circuit for quantum state transformation, combined with a fidelity-based cost function for model optimization, offers a more precise and adaptable solution than traditional methods. The implementation of the quantum Fourier transform and Toffoli gates for state manipulation also introduces an innovative approach to quantum environmental monitoring.

3. Problem statement

This paper addresses three interrelated aspects: (1) transforming sensor data into a quantum-compatible format, (2) using a VQC for accurate prediction of gas concentrations, and (3) leveraging quantum

Table 1
A summary of quantum computing applications in networks.

Ref.	Key feature	Advantage	Disadvantage	Challenge addressed
[20]	Entanglement swapping, repeater chains optimization	Enhanced entanglement distribution efficiency	Non-associative nature of quantum repeater chains	Optimization in quantum repeater chains
[25]	Quantum transportation modeling	Accuracy in transportation planning	Quantum adaptation of methods	Quantum transportation
[26]	Edge server placements in IoVs with quantum encoding	Scalability of edge server placement in IoVs	Computational intensity	Edge server placements and resource management
[27]	Quantum approximate algorithm	Faster routing path identification	Quantum hardware ecosystem	Quantum Vehicular routing
[28]	Federated quantum neural network	Resource optimization and privacy	Neural network complexity	Quantum Wireless communication
[29]	NFTs with quantum RL	Secure data sharing in IoVs	Scalability issues in IoVs	Resource allocation and security
[30]	Asynchronous entanglement distribution protocol	Robust quantum entanglement distribution	Complexity compared to synchronous alternatives	Coordination in quantum networks
[10]	Quantum–classical hybrid method	Accurate sensor placement	Technological complexity	Vehicular sensor placement
[33]	QML for database query processing	Reduced query processing time	Scalability and reliability issues	Optimizing join order in queries
[34]	quantum-inspired RL in IoVs	Effective resource management	Computing limitations	Resource management in IoVs

entanglement for near real-time transmission of hazard alerts. The transformation of classical sensor data $\mathbf{S}$, representing gas concentrations detected by vehicles, into a quantum state $|\lambda\rangle$ in a Hilbert space is achieved through a rotational transformation $\mathbb{R}_\theta(\mathbf{S})$, applied to an initial state $|\lambda_0\rangle$:

$$|\lambda\rangle = \mathbb{R}_\theta(\mathbf{S})|\lambda_0\rangle \tag{1}$$

This quantum state enables further processing through the VQC, which predicts hazard levels based on $|\lambda\rangle$. The VQC utilizes a quantum circuit $U(\mathbf{\Phi})$, where $\mathbf{\Phi}$ represents adjustable parameters, to map the sensor data $\mathbf{S}$ to the probability of hazard levels:

$$P(\text{hazard level}|\mathbf{S}) = \text{Tr}\left[\Pi \cdot U(\mathbf{\Phi})|\lambda\rangle\langle\lambda|U^\dagger(\mathbf{\Phi})\right] \tag{2}$$

Here, Π is the projector for hazard levels, and Tr denotes the trace operation, ensuring accurate classification. To enable rapid alert transmission, the network utilizes quantum entanglement, modeling vehicles as a multipartite entangled state $|\Psi\rangle$. Through quantum teleportation, hazard alerts encoded in $|\lambda\rangle$ are transmitted to target vehicles or control centers:

$$|\lambda\rangle_{\text{target}} = \sigma_x^a \sigma_z^b (I \otimes \langle\beta_{ab}|)(|\lambda\rangle \otimes |\Psi\rangle) \tag{3}$$

where $\langle\beta_{ab}|$ represents the Bell state measurement, and σ_x, σ_z are Pauli matrices with measurement outcomes a and b guiding the teleportation. This process ensures rapid and reliable hazard alerts throughout the network. The overall system's performance is optimized through a multi-component objective function $\mathcal{L}(\theta, \rho, \tau)$, which balances quantum state fidelity, prediction accuracy, and communication latency:

$$\begin{aligned}\mathcal{L}(\theta, \rho, \tau) = \alpha \sum_{i=1}^{N} \left(1 - F\left(\rho_i, \hat{\rho}_i(\theta)\right)\right) \\ + \beta \sum_{j=1}^{M} \text{CE}\left(P\left(y_j|\hat{\rho}_j(\theta)\right), y_j\right) + \gamma \sum_{k=1}^{K} \tau_k,\end{aligned} \tag{4}$$

where θ denotes the variational parameters, ρ_i is the true quantum state, $\hat{\rho}_i(\theta)$ is the predicted state, and τ_k represents communication latency. The coefficients α, β, and γ adjust the focus on information preservation, prediction accuracy, and near real-time responsiveness. This objective function guides the system to ensure high-fidelity predictions and timely alert transmission, offering a robust framework for hazardous gas monitoring in vehicular networks.

4. Architectural design

Fig. 2 illustrates the environmental monitoring model, which leverages quantum computing to process data collected from vehicle-mounted sensors. The data is first normalized and then encoded into quantum states, ensuring compatibility with quantum computational processes. This approach creates a sophisticated, multifaceted system designed to meet the complex requirements of contemporary environmental monitoring.

4.1. Data collection and quantum state encoding

Each vehicle is equipped with a range of sensors (see Fig. 3), including MQ2, MQ3, MQ5, MQ6, MQ7, MQ8, MQ135, and GPS, to provide comprehensive air quality assessment and location tracking. These sensors constitute the core monitoring capabilities of the QMF. After data collection, sensor readings are normalized to ensure compatibility with quantum computing processes. The standardized data is then encoded into quantum states $|\lambda\rangle$, which can exist in multiple superpositions simultaneously. This encoding, defined by the function $E : S \to |\lambda\rangle$, is essential for transforming conventional sensor data into a quantum-compatible format suitable for processing. Here, $|\lambda_0\rangle$ denotes the all-zero initial quantum state (e.g., $|0 \cdots 0\rangle$ of n qubits), and $R_\theta(S)$ is a rotation operator that maps the normalized sensor data S to a set of qubit rotation angles. In practice, each sensor reading is encoded as a rotation angle θ_i on a corresponding qubit, so that the operation $R_\theta(S)$ transforms $|\lambda_0\rangle$ into the quantum state $|\lambda\rangle$ in an n-qubit Hilbert space, encoding the multi-sensor data in quantum superposition.

4.2. Hardware feasibility

qIoV is conceived as a forward-looking architecture, requiring certain advances in quantum technology. It assumes each vehicle is equipped with a multi-gas sensor suite and a compact quantum communication module. Recent strides in photonic integration have yielded smaller, more robust quantum devices [36]. We anticipate that only lightweight components (entangled-photon sources, single-photon detectors, etc.) need to be vehicle-mounted, while intensive quantum processing is offloaded to edge or cloud quantum servers. The vehicle's

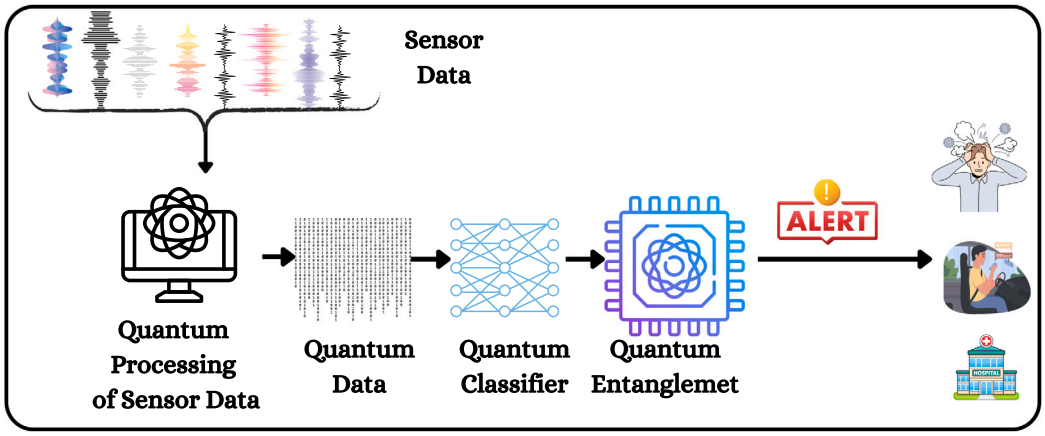

Fig. 2. Quantum process for qIoV framework.

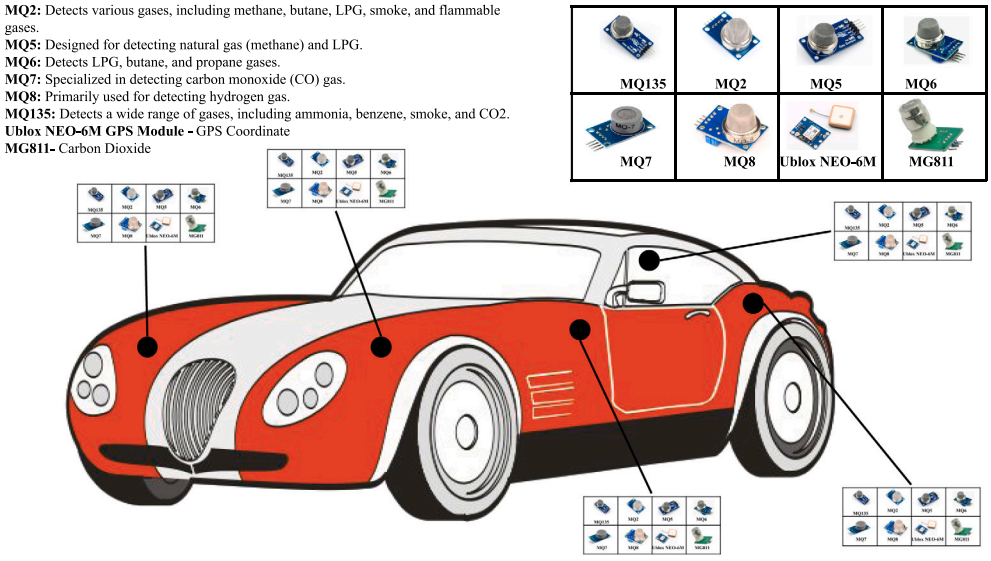

Fig. 3. Environmental sensing using vehicular sensors.

quantum hardware would reside in a stabilized enclosure (shock-mounted and thermally insulated) to ensure stable operation under motion. Standard vehicular power is sufficient to cool and run these devices, and each vehicle carries multiple gas sensors (e.g., MQ2, MQ3, …, MQ135) to detect a range of toxins.

The current technology imposes some strict limits. Entangled states maintain coherence only on the order of microseconds to milliseconds without special quantum memory. At typical city driving speeds (≈ 15 m/s) and line-of-sight distances of a few hundred meters, a direct entangled link between two moving vehicles would remain viable for only a few seconds before relative motion or obstructions degrade the channel. Thus, the QMF must redistribute entanglement on the order of every 1–5 s per link in dense traffic. This refresh rate (0.2–1 Hz) implies the network must continuously generate and distribute entangled pairs at a similar rate to sustain a high-fidelity multipartite state. Additionally, we assume future improvement in quantum operation fidelity. qIoV's stabilizer-based error correction requires physical gate error rates on the order of 10^{-3} (0.1%) or better to significantly boost entanglement fidelity. Present quantum hardware is only beginning to approach this range. The current 127-qubit superconducting processor has two-qubit gate errors around 1%–2% and ≈100 μs coherence time, meaning true fault-tolerant operation is not yet achievable. In our simulations, we therefore employed error mitigation techniques (instead of full error correction) and kept quantum circuits shallow to work within these limits.

4.3. Quantum graph and network state representation

The vehicles are modeled as quantum entities, forming a dynamic quantum graph $\mathcal{G}(t)$, where the nodes correspond to state vectors in the Hilbert space $\mathcal{H}$, and the edges represent potential quantum entanglements. The network's overall entangled state at time t can be represented by a density matrix $\rho(t)$. Its evolution can be modeled (in principle) by a Lindblad master equation, which formalizes how environmental interactions (noise, vehicular motion, etc.) cause the state to decohere over time. We do not delve into formalism here, but note that as time progresses, such decoherence will gradually degrade the shared entangled state, motivating an active management approach.

The QMF serves as a dedicated quantum communication backbone that dynamically preserves quantum links amidst vehicular motion and urban interference. Rather than relying on any single entangled pair to remain coherent, QMF continuously refreshes and swaps entanglements as needed. It distributes entangled qubit pairs to vehicles via nearby quantum nodes and monitors link fidelity in real time. If an entangled link starts to decohere or is interrupted (due to vibrations, loss of line-of-sight, etc.), the fabric quickly replaces it by either establishing a

fresh entangled pair or performing entanglement swapping through an intermediate node. In this way, an up-to-date entangled channel is always available for each vehicle, effectively extending the usable entanglement lifetime despite mobility. To further safeguard entanglement, each vehicle's quantum transceiver is housed in a stabilized unit that dampens vibration and maintains thermal control, reducing environment-induced phase noise. The entangled communication uses optical channels (fiber-optic or free-space laser links), which are immune to radio-frequency interference. Thus, qIoV operates as an overlay: its quantum links run in parallel on a separate optical spectrum, augmenting the conventional V2X network without disrupting it. In dense urban areas with frequent occlusions, QMF leverages multi-hop entanglement: a vehicle that loses direct line-of-sight entanglement can connect via a relay (e.g., a roadside quantum node or another vehicle). The entangled state is swapped through one or more such relays so that, even if direct paths are blocked by buildings, the end vehicles remain entangled via alternate routes. This is analogous to routing around a dropped link in classical networks, except here the rerouting is achieved by quantum entanglement swapping rather than packet forwarding.

Scalability and Integration: The entanglement management scheme is designed to scale efficiently as the vehicular network grows. Rather than trying to entangle every pair of vehicles (which becomes intractable for large N), QMF organizes vehicles into entangled clusters (cells). Within each cluster (on the order of tens of vehicles), members share multipartite entangled states or a network of Bell pairs. Entanglement swapping is then used to connect these clusters hierarchically. This structured approach bounds the complexity: as N rises to hundreds or thousands, QMF dynamically entangles local neighbors and links clusters via a few connector nodes, avoiding an explosion of entangled connections. A central quantum server (or multiple regional quantum nodes) coordinates entanglement distribution so that even in a large fleet, any given vehicle can quickly obtain entanglement with the network. Over extended distances, quantum repeaters (or satellite-based quantum links) will be necessary as intermediate nodes to extend range and counteract photon loss and decoherence. By deploying such repeaters (e.g., at telecom fiber hubs or on airborne platforms), QMF can maintain high-fidelity entanglement between far-flung vehicles without requiring direct line-of-sight for every link. In essence, qIoV's quantum network scales by forming an entangled backbone of clusters.

4.4. Mobility and communication model: Quantum teleportation

In qIoV, hazardous gas detection begins with quantum sensing via an Entangled Quantum Feature Map (EQFM), which encodes the 7-channel vehicular gas vectors into a strongly entangled qubit register through layered CZ interactions. This preserves high-order cross-sensor dependencies that classical embeddings miss and feeds the representation into a variational classifier optimized directly for state fidelity. The noise-aware ansatz, combining iSWAP/CPHASE gates with adaptive single-qubit rotations maintains expressive power under realistic error while keeping circuits compact.

Detected hazards are disseminated through a QMF, which pre-distributes Bell pairs between vehicles and control servers, refreshes links via mobility-aware entanglement swapping, and teleports encoded hazard states $|\lambda\rangle$ to their destinations. In the teleportation step, the hazard state is entangled with the network's multipartite state $|\Psi\rangle$ and measured in the Bell basis, producing two classical bits. These bits, sent over a conventional channel at light speed (fiber/wireless), instruct the receiver, holding the pre-shared entangled qubit on which Pauli X and Z operations to apply, reconstructing $|\lambda_{\text{target}}\rangle$ with near-unity fidelity.

Since only the classical bits traverse the network, the latency is bounded to microseconds–milliseconds over urban distances, negligible relative to human reaction times and compliant with causality. This tight integration of (i) entanglement-aware feature mapping with QFT-assisted embedding and (ii) teleportation-based, mobility-adaptive alert dissemination is unique among IoV sensing frameworks. The approach's added complexity and cost are justified in high-dimensional, weak-signal regimes, where qIoV delivers clear class separation, high precision/recall, and faster end-to-end detection even under high network overhead.

Mobility and Connectivity Dynamics: In a vehicular quantum network, node mobility plays a decisive role in connectivity. As vehicles move, previously established entangled links may decohere or be lost. If line-of-sight is blocked or if the inter-vehicle distance exceeds the quantum channel's range. Our qIoV framework treats entangled links as dynamic, ephemeral resources. At any time t, the network's entanglement graph can fragment due to vehicle motion. We introduce a simple mobility model to quantify entanglement link lifetimes. Consider vehicles moving with an average speed of ≈40 km/h and a quantum communication range of ≈200 m (typical in urban settings). Under these conditions, an entangled link between two vehicles would on average persist only on the order of a few seconds (e.g., 2–5 s in moderate traffic) before the vehicles move out of range or an obstruction intervenes. After that, the entangled connection would break and need reconfiguration. When a vehicle's entangled link terminates due to motion, the QMF responds much like a classical network recovering from a dropped connection. It rapidly performs entanglement swapping or distributes a new entangled pair via an alternate route. For example, if Vehicle A and Vehicle B lose their direct entanglement (say, A drives out of range of B), QMF enlist an intermediate node, Vehicle C or a roadside quantum repeater that still has entangled links with both A and B to swap entanglement. Through this relay, A and B become indirectly entangled (A-C and C-B effectively form an A-B link). This quantum re-routing happens behind the scenes and in advance, ensuring that when one path fades, another entangled path is readily available. The process is analogous to a handoff in cellular networks or a routing update in VANETs, except here we are rerouting quantum states instead of packet flows.

Routing Behavior and Latency: In classical IoV networks, a broken link triggers a routing protocol to find a new multi-hop path, incurring delays at each hop. By contrast, qIoV's strategy is to maintain a web of entangled links, a quantum overlay, so that if one path is disrupted, quantum information can be instantly redirected through another entangled route. The act of teleportation (transmitting an alert quantum state via entanglement) has negligible latency: only two classical bits need to be sent to complete the teleportation, which over metropolitan distances takes mere microseconds. The main delay when a link is lost is the time to establish a new entangled pair. Using today's technology figures, distributing a fresh entangled photon pair (including any required optical switching) can be done on the order of milliseconds. This re-entanglement delay is very small, often comparable to or below the latency of a single wireless hop in classical networks. It does introduce a slight variability in end-to-end alert delivery time (since occasionally a vehicle may need to wait those few milliseconds for a new entangled link), but the baseline latency remains extremely low.

Channel Reliability and Deployment Considerations: Environmental factors, i.e., heavy rain, fog, or physical occlusions by buildings and other vehicles can disrupt optical quantum links. qIoV leverage a multi-tier infrastructure, if a direct vehicle-to-vehicle quantum channel fails, vehicles can fall back on infrastructure nodes such as roadside quantum units. These infrastructure nodes ensure that even fast-moving or distant vehicles can share entanglement via multi-hop routes that circumvent local blockages. Naturally, each extra hop or swap will introduce additional decoherence and reduce the entangled state's fidelity. A decaying fidelity term is introduced in our network model (using a Lindblad master equation framework) to represent how quantum state $\rho(t)$ degrades with each such operation over time. To counteract this, the QMF employs quantum error management techniques. It continuously monitors entangled link fidelity (using stabilizer measurements on entangled qubits). If the fidelity drops below a set threshold due to motion-induced decoherence or transmission loss, the

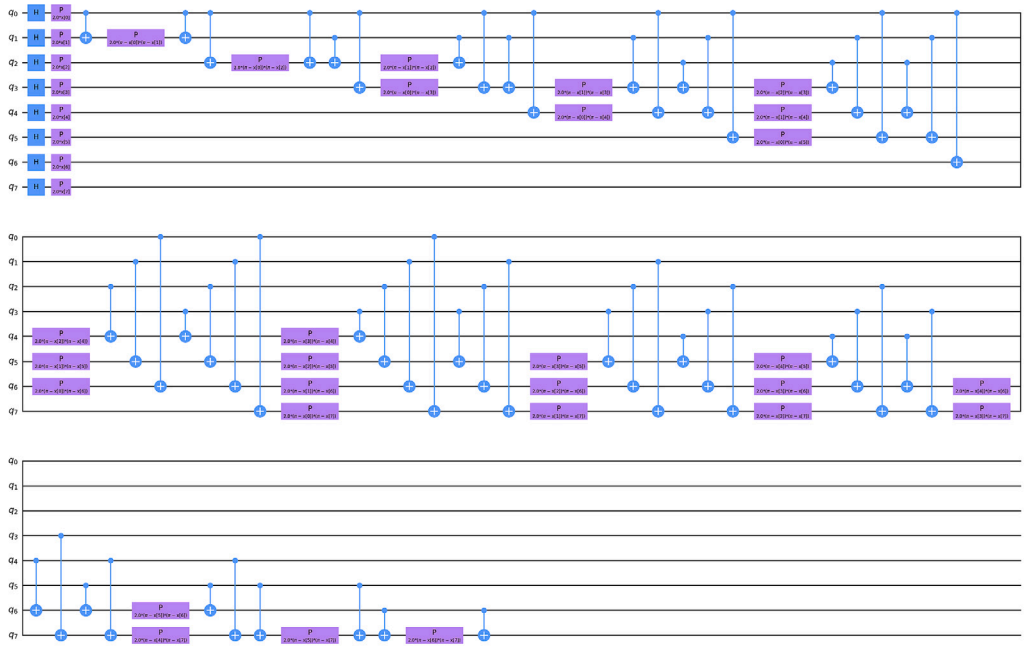

Fig. 4. Entangled quantum feature map for advanced data encoding.

affected entangled link is proactively repaired or replaced. QMF can invoke an entanglement purification protocol to improve fidelity, or simply discard the low-fidelity pair and distribute a new high-fidelity entangled pair in its place. In extreme cases, quantum error-correcting codes used to sustain entanglement over longer durations, though these incur overhead. The system is designed such that transient failures or fluctuations in channel quality do not collapse the entire network's entangled state, the entanglement can be rapidly rerouted or restored through alternate paths and fresh resources.

5. Proposed methodology

This section outlines our framework, focusing on three key processes: data conversion, entanglement-based communication, and error management. First, multi-dimensional sensor data is transformed into quantum-compatible states using an optimized encoding scheme that adjusts rotation angles to accurately capture distinct environmental sensor patterns. Next, we implement a multipartite entanglement strategy tailored for vehicular networks, enabling rapid and reliable dissemination of environmental alerts through quantum teleportation with vehicle-specific entanglement patterns. To mitigate quantum noise and computational errors in dynamic vehicular environments, we employ adaptive quantum circuit optimization, utilizing stabilizer codes for error detection and correction while adjusting quantum gate parameters to maintain communication fidelity. These integrated processes create a robust quantum-enhanced system for environmental monitoring and hazard alert dissemination within vehicular networks.

5.1. Quantum data and encoding and conversion

Environmental data is collected from vehicle-mounted sensors MQ2, MQ3, MQ5, MQ6, MQ7, MQ8, and MQ135, generating time-series datasets $x_1, x_2, \ldots, x_7$. These datasets are organized into a matrix $\mathbf{S} \in \mathbb{R}^{m\times n}$, where m represents the time-dependent data points for each sensor, and n corresponds to the sensors. Each column of $\mathbf{S}$ contains time-series data from a specific sensor x_i, while each row captures the readings from all sensors at a particular time instant.

5.1.1. Normalization process

Standardization is essential to ensure consistency across the varied sensor data $\mathbf{S}_i$, aligning it with quantum state representation. We use Min–Max normalization, defined as:

$$s'_{ij} = \frac{s_{ij} - \min(\mathbf{S}_i)}{\max(\mathbf{S}_i) - \min(\mathbf{S}_i)} \tag{5}$$

where s_{ij} is the raw data from the ith time point of the jth sensor, and s'_{ij} is the normalized value. $\min(\mathbf{S}_i)$ and $\max(\mathbf{S}_i)$ represent the minimum and maximum values of the jth sensor's time-series data. This process scales readings to the $[0, 1]$ range, ensuring a consistent data format for accurate quantum state encoding and processing.

5.1.2. Quantum state encoding via entangled feature mapping

We employ an EQFM to encode sensor data into a quantum state, leveraging entanglement for enhanced data representation (see Fig. 4). The first layer of the quantum circuit applies Hadamard gates, placing qubits in superposition, followed by parameterized phase gates $P(\boldsymbol{\Psi}_i)$, which introduce feature-dependent phase shifts. Controlled-Z (CZ) gates, arranged in layers, maximize entanglement to capture feature correlations. Each entanglement layer uses cascading CZ gates between qubits, with phase parameters $P(2\theta_i - 2\theta_j - \theta_k)$ determined by input data. Multiple layers of this structure allow the quantum state to capture higher-order correlations, crucial for preserving complex data patterns. The EQFM transforms normalized sensor data into an entangled quantum state via the unitary transformation $U_\theta^E(\boldsymbol{\Psi})$:

$$U_\theta^E(\boldsymbol{\Psi}) = \bigotimes_{i=1}^{7} \left(H_i \cdot CZ_{i,t}(\boldsymbol{\Psi}_i) \right). \tag{6}$$

Here, Hadamard gates H_i create superpositions, while controlled-Z gates $CZ_{i,t}$ entangle qubits based on the input data. This ensures the encoded quantum state preserves both individual feature information and their interdependencies, making it suitable for processing by VQC. Further, our layered entangling feature map effectively encodes higher-order correlations among the sensor inputs into the quantum state. By using multi-qubit gates (e.g., controlled-Z rotations) that entangle multiple qubits at once, the mapping ensures that joint variations in sensor readings influence the state. For example, an entangling operation with a phase parameter $(2\theta_i - 2\theta_j - \theta_k)$ couples the quantum

state's evolution to the combined values of sensors i, j, and k. Such terms mean the resulting quantum state is a superposition embedding not only individual sensor information but also their interdependencies (e.g. pairwise and triple-wise relationships) directly in the amplitudes. Therefore, unlike a feature mapping that treats each sensor separately, the EQFM preserves higher-order sensor relationships in the data representation. This richer encoding increases the model's expressive power. The data has been lifted into a high-dimensional Hilbert space where relevant patterns can be more easily separated. This eases the learning task for the VQC. Because the essential multi-sensor features are already entangled into the quantum state, the VQC can find a decision boundary with fewer circuit layers and fewer training iterations than a classical model would likely require.

5.1.3. Parameterized ansatz for quantum state evolution

We utilize a parameterized ansatz circuit $|\omega(\boldsymbol{\theta})\rangle$ (see Fig. 5) for quantum state transformation. The circuit integrates multi-qubit gates (iSWAPs, CPHASE) along with adaptive single-qubit rotations, enabling advanced quantum state manipulation. We selected the quantum circuit in Fig. 5 deliberately to balance expressive power and viability on quantum hardware. This variational ansatz comprises on the order of tens of gates (approximately 30 single-qubit rotations and 20 two-qubit entangling operations in total per full circuit layer). This circuit was chosen because it can capture high-order correlations among the seven sensor features that simpler circuits would miss. In particular, the inclusion of multi-qubit gates (iSWAP and CPHASE in each layer) allows the ansatz to entangle qubits representing different sensors' data, thereby exploring a larger portion of the Hilbert space. The transformation of sensor data through this ansatz is expressed as:

$$|\omega(\boldsymbol{\theta})\rangle = U^{(m)}_{\text{dynamic}}(\boldsymbol{\theta}_{\text{dynamic}}) \cdot U^{(m)}_{\text{multi-qubit}}(\boldsymbol{\theta}_{\text{multi-qubit}}). \tag{7}$$

Here, $U^{(m)}_{\text{dynamic}}(\theta_{\text{dynamic}})$ represents m layers of sequential single-qubit rotations (dynamic, parameterized gates that can adapt to error syndromes), and $U^{(m)}_{\text{multi-qubit}}(\theta_{\text{multi-qubit}})$ represents m layers of multi-qubit entangling operations (such as iSWAP and CPHASE gates). Together, these two unitary components form the ansatz circuit that transforms the state. This layered ansatz structure ensures that the quantum state $|\omega(\theta)\rangle$ can explore a rich Hilbert space for optimal representation of the sensor data. However, each additional gate (especially two-qubit gates) increases the opportunity for error. To mitigate these effects, our framework incorporates adaptive and noise-aware design elements. Notably, the single-qubit rotation gates in the ansatz are dynamic, meaning their parameters can adjust in response to observed error syndromes. Moreover, during simulation we applied error mitigation strategies: depolarizing noise was included in the OpenQASM tests, and the variational parameters were optimized while accounting for this noise. This approach effectively "leans into" the noise, the training process seeks parameter values that yield correct classification results despite gate errors.

5.1.4. Quantum data transformation technique

Our framework encodes the normalized sensor data $\mathbf{S}'$ into quantum states using a mapping function $h : \mathbf{S}' \to \vec{\theta}$, which converts data points into rotation angles for efficient quantum circuit utilization. For each qubit q_i, the rotation gate $R(\theta_i)$ is expressed as:

$$R(\theta_i) = \begin{pmatrix} \cos(\theta_i) & -i\sin(\theta_i) \\ -i\sin(\theta_i) & \cos(\theta_i) \end{pmatrix}. \tag{8}$$

This gate enables precise data encoding, with the adaptive mapping function h optimizing the representation of sensor data in the quantum domain.

5.1.5. Quantum encoding and state preparation

The encoding of sensor data into a quantum state $U(\mathbf{S}')$ involves both single and multi-qubit rotations, generating the quantum state $|\lambda(\boldsymbol{\theta})\rangle$, which is essential for quantum computations. The encoding process is represented as:

$$U(\mathbf{S}')z = \bigotimes_{i=1}^{n} R(\theta_i(s'_i)), \tag{9}$$

Here, the initial state $|\lambda\rangle_0$ evolves into the encoded state $|\lambda\rangle$, where accurate calculation of θ values is critical for maintaining state fidelity.

5.2. Modified quantum variational classifier

This section details the VQC's internal mechanisms, covering its design and practical implementation. The VQC implementation involves a multi-stage process: initially, conventional sensor data is transformed into a quantum-compatible format. We then evaluate the model's accuracy using a fidelity-based cost function, followed by the application of an advanced optimization technique to enhance overall performance.

5.3. Algorithmic overview

The implementation details of the VQC is presented in *Algorithm* 1, including fundamental steps:

Algorithm 1 VQC with Adaptive Optimization

Input: Sensor data $\{x^{(i)} = (x_1^{(i)}, x_2^{(i)}, \ldots, x_7^{(i)})\}_{i=1}^{N}$, Variational parameters $\boldsymbol{\theta}$, Number of layers M
Output: Predicted gas types for given sensor data
for $i = 1$ to N **do**
  Encode sensor data into quantum states: $|\lambda^{(i)}(\boldsymbol{\theta})\rangle \leftarrow U^{(M)}_{\text{entangle}}(\boldsymbol{\theta}_{\text{entangle}}) \cdot U^{(M)}_{\text{rotation}}(\boldsymbol{\theta}_{\text{rotation}})|0\rangle^{\otimes n}$
end for
Initialize cost function: $C(\boldsymbol{\theta}) \leftarrow 0$
for $i = 1$ to N **do**
  Execute quantum circuit: $U(\boldsymbol{\theta})|\lambda^{(i)}(\boldsymbol{\theta})\rangle$
  Measure probabilities $P(y_j|\boldsymbol{\theta})$ for gas classes y_j
  Calculate fidelity $F(|\lambda^{(i)}_{\text{expected}}\rangle, U(\boldsymbol{\theta})|\lambda^{(i)}(\boldsymbol{\theta})\rangle)$
  Update cost function: $C(\boldsymbol{\theta}) \leftarrow C(\boldsymbol{\theta}) + (1 - F(|\lambda^{(i)}_{\text{expected}}\rangle, U(\boldsymbol{\theta})|\lambda^{(i)}(\boldsymbol{\theta})\rangle))^2$
end for
Optimization:
Set initial learning rate η, threshold ϵ, and maximum iterations K
Initialize $\boldsymbol{\theta}_0$ randomly
$k \leftarrow 0$
while $k < K$ or $\Delta C(\boldsymbol{\theta}_k) > \epsilon$ **do**
  Calculate gradient $\nabla C(\boldsymbol{\theta}_k)$
  Adjust learning rate: $\eta_k \leftarrow \eta/(\sqrt{k+1})$
  Update parameters: $\boldsymbol{\theta}_{k+1} \leftarrow \boldsymbol{\theta}_k - \eta_k \nabla C(\boldsymbol{\theta}_k)$
  $k \leftarrow k + 1$
end while
return Predicted gas types based on optimized $\boldsymbol{\theta}$

5.3.1. Quantum state encoding

For classical sensor data $x^{(i)} = (x_1^{(i)}, x_2^{(i)}, \ldots, x_7^{(i)})$ across N instances, we construct the corresponding quantum state $|\lambda^{(i)}(\boldsymbol{\theta})\rangle$ using parameterized quantum circuits that represent the sensor data within the quantum domain:

$$|\lambda^{(i)}(\theta(x^{(i)}))\rangle = U^{(M)}_{\text{entangle}}\left(\theta_{\text{entangle}}(x^{(i)})\right) \cdot U^{(M)}_{\text{rotation}}\left(\theta_{\text{rotation}}(x^{(i)})\right)|0\rangle^{\otimes n}, \tag{10}$$

Here, $U^{(M)}_{\text{entangle}}(\boldsymbol{\theta}_{\text{entangle}})$ and $U^{(M)}_{\text{rotation}}(\boldsymbol{\theta}_{\text{rotation}})$ represent the entangling and single-qubit rotation gates with M layers, parameterized by $\boldsymbol{\theta}_{\text{entangle}}$ and $\boldsymbol{\theta}_{\text{rotation}}$, respectively.

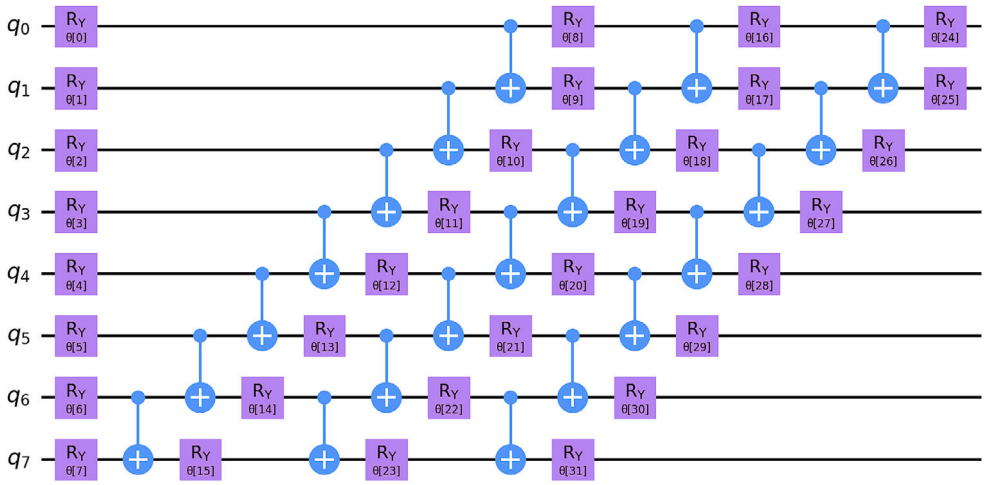

Fig. 5. Enhanced ansatz circuit for quantum state evolution.

5.3.2. Cost function formulation

In quantum computing, a fidelity-based cost function assesses how accurately our quantum model's predictions align with expected outcomes, effectively quantifying model accuracy. The cost function $C(\boldsymbol{\theta})$ is defined to measure the discrepancy between expected and observed quantum states:

$$C(\boldsymbol{\theta}) = \sum_{i=1}^{N} \left(1 - F(|\lambda^{(i)}_{\text{expected}}\rangle, U(\boldsymbol{\theta})|\lambda^{(i)}(\boldsymbol{\theta})\rangle)^2\right), \tag{11}$$

Here, $|\lambda\_\text{expected}^{(i)}\rangle$ denotes the ideal quantum state corresponding to the true class of the ith sensor sample. We assign each gas type to a distinct computational basis state in the quantum output space. For example, if $L = 4$ hazard classes are encoded using $n = 2$ qubits ($2^n \geq L$), and a given training sample belongs to class $j = 2$, the expected state is prepared as $|\lambda\_\text{expected}^{(i)}\rangle = |10\rangle$ (the basis state with binary representation '10'). The fidelity $F(|\lambda\_\text{expected}^{(i)}\rangle, ; U(\theta), |\lambda^{(i)}(\theta)\rangle)$ thus quantifies the overlap between the VQC's output state and the correct class-j state. By optimizing this fidelity-based cost, the VQC is trained to produce quantum states that closely match the expected class states for each input.

5.3.3. Adaptive optimization scheme

Our optimization scheme uses an iterative process to incrementally refine the model. At each iteration, the learning rate η_k is adjusted to ensure steady and efficient convergence:

$$\boldsymbol{\theta}_{k+1} = \boldsymbol{\theta}_k - \eta_k \nabla C(\boldsymbol{\theta}_k), \tag{12}$$

where $\nabla C(\boldsymbol{\theta}_k)$ denotes the gradient of the cost function with respect to the variational parameters. The integration of quantum state encoding, the fidelity-based cost function, and adaptive optimization establishes a robust framework for fine-tuning these parameters based on fidelity changes. This approach effectively captures subtle variations in quantum states derived from sensor data, enabling accurate gas-type predictions.

5.3.4. Extensive quantum state processing and measurement for hazard level assessment

After training, the VQC applies its optimized circuit to newly encoded quantum sensor data $|\lambda\rangle$. The resulting state $|\lambda'\rangle$, given by $U(\boldsymbol{\Phi})|\lambda\rangle$, reflects the VQC's analysis of toxic gas concentrations. To extract actionable insights, $|\lambda'\rangle$ is measured using a set of projective operators $\{\Pi_i\}$, each representing a specific hazard level. The probability of each hazard level, based on the sensor data, is determined as:

$$P(\text{hazard level}_i|\mathbf{S}) = \text{Tr}\left[\Pi_i \cdot U(\boldsymbol{\Phi})|\lambda\rangle\langle\lambda|U^{\dagger}(\boldsymbol{\Phi})\right]. \tag{13}$$

This integrated process of data encoding, quantum circuit construction, training, and execution demonstrates the VQC's effectiveness in predicting toxic gas levels, underscoring its potential in early hazard detection.

5.4. Quantum entanglement process

Quantum entanglement, a fundamental phenomenon in quantum physics, is central to the functionality of our qIoV framework, which supports secure communication in vehicular networks for hazardous gas monitoring. Entanglement refers to the phenomenon where the state of one particle affects its entangled counterpart, regardless of distance.

Our model uses quantum entanglement and teleportation for near real-time, secure data transmission, as illustrated by the three-qubit quantum circuit in Fig. 6. Bell State Preparation entangles qubits, assigning each vehicle a quantum identifier i and its corresponding server qubit j within a network of n vehicles:

$$|\Psi\rangle_i \xrightarrow{\text{Bell}} \frac{1}{\sqrt{2}}(|00\rangle + |11\rangle)_{i,n+j}. \tag{14}$$

This transition into a Bell state, which encodes information more effectively than Hadamard gates, is represented as:

$$|\Psi\rangle_i \xrightarrow{\text{Bell}} \frac{1}{\sqrt{2}}(|00\rangle + |11\rangle)_{i,j}. \tag{15}$$

Next, the Quantum Fourier Transform (QFT) manipulates entangled states for data embedding and transfer:

$$|\Psi\rangle_i, |\Psi\rangle_{i+1} \xrightarrow{\text{QFT}} QFT(|\Psi\rangle_i), QFT(|\Psi\rangle_{i+1}). \tag{16}$$

As shown in Fig. 6, the circuit begins with Bell state preparation using U_2 and controlled-NOT (CX) gates, entangling vehicle and server qubits. Phase gates $P(\theta)$, with values such as $\pi/8$ and $-\pi/8$, then encode data onto the quantum state. Hadamard gates create superposition states, allowing efficient quantum state manipulation.

The QFT, crucial for data embedding, spreads quantum information across qubits, preparing the state for teleportation and phase estimation. Controlled-phase gates create the quantum correlations necessary

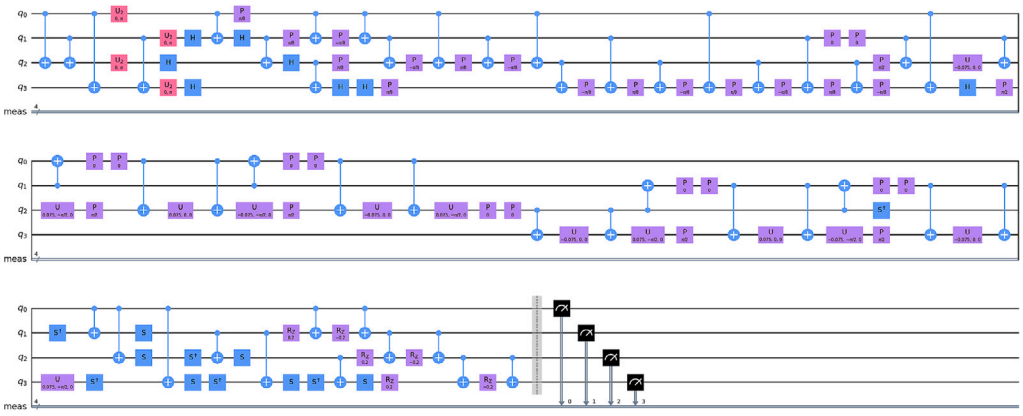

Fig. 6. Quantum circuit representation of communication.

for data transmission, while S and $S^{\dagger}$ gates maintain phase coherence. To enable reliable communication, a Toffoli gate provides multi-qubit control, facilitating quantum teleportation. The process concludes with a controlled-Z rotation gate $R_Z(\theta)$ for precise phase manipulation:

$$R_Z(\theta) = \begin{pmatrix} 1 & 0 \\ 0 & e^{i\theta} \end{pmatrix} \tag{17}$$

Finally, measurement gates retrieve the classical information embedded in the quantum states, representing the transmitted sensor data for analysis within the vehicular network.

Algorithm 2 Quantum Communication Protocol

Require: vehicle count (n), number of rounds (R), quantum register size per vehicle (m)
Ensure: Quantum communication protocol
1: Initialize a quantum circuit with $3m = 3n$ qubits.
2: **for** $r_i = 1$ to R **do**
3: **for** each vehicle v_i, $i = 1$ to n **do**
4: Prepare Bell state for qubits $(3i-2, 3i-1)$: $|\Psi\rangle_{3i-2,3i-1} \xrightarrow{\text{Bell}} \frac{1}{\sqrt{2}}(|00\rangle + |11\rangle)$
5: Apply QFT on the third qubit of each vehicle: $|\Psi\rangle_{3i} \xrightarrow{\text{QFT}} QFT(|\Psi\rangle_{3i})$
6: **end for**
7: **for** each pair of vehicles (v_i, v_j), $i \neq j$ **do**
8: Apply Toffoli gate to strengthen quantum correlations: Toffoli$(|\Psi\rangle_{3i-1}, |\Psi\rangle_{3j-1}, |\Psi\rangle_{3i})$
9: Apply QPE for precise phase calculations: QPE$(|\Psi\rangle_{3i}, |\Psi\rangle_{3j})$
10: **end for**
11: **for** each vehicle v_i **do**
12: Perform Quantum Teleportation using a controlled-Z rotation gate: Teleport$(|\Psi\rangle_{3i-2}, |\Psi\rangle_{3i-1}, |\Psi\rangle_{3i})$
13: **end for**
14: **end for**
15: Measure all qubits.
16: Transpile the circuit for optimization.
17: **return** Quantum circuit representing the communication protocol.

6. Performance evaluation

This section evaluates the qIoV framework, highlighting its effectiveness in accurately detecting toxic gases from vehicle-mounted sensor data. The pair plot method was crucial for analyzing data correlations and enhancing detection accuracy. Additionally, we assessed quantum data distributions under varying conditions using a 127-qubit system on the IBM OpenQASM 3 platform. Note that this 127-qubit system refers to a simulated quantum environment realized through IBM's OpenQASM 3 framework, rather than a physical quantum computer with 127 qubits. We used this simulation platform to emulate a large-scale quantum circuit corresponding to our network, given that current quantum hardware with this many qubits is not readily available for full experiments.

6.1. Simulation environment and implementation details of VQC

Experiments were conducted by designing a parameterized quantum circuit for the VQC using the quantum circuit composer on the OpenQASM 3 platform. We arranged Hadamard, Pauli-X, Controlled-Z, and rotation gates to create an entangled state that effectively captured the complexity of the sensor data. Sensor data encoding was achieved through a customized quantum feature map, converting classical gas concentration readings into quantum states. The fidelity-based cost function was assessed by measuring the overlap between the VQC's output state and the ideal state for accurate gas classification. Parameter updates were carried out using a gradient-based optimization algorithm, with gradients estimated via the parameter-shift rule. We trained the VQC using gradient descent. The initial learning rate was $\eta = 0.1$, and we employed an adaptive schedule $\eta\_k = \eta/\sqrt{k+1}$ to gradually decrease the learning rate each iteration for stable convergence.

All of our quantum experiments were executed in simulation, using IBM's OpenQASM 3 framework on a Qiskit-based backend. We modeled a notional 127-qubit quantum processor to emulate a large-scale device (corresponding to IBM's 127-qubit Eagle architecture). Our circuits utilized far fewer qubits (typically 10–20 qubits active), but the simulator's capacity allowed us to include up to 127 virtual qubits if needed for entanglement distribution. We also incorporated a realistic noise model into all simulations to reflect hardware constraints. Single-qubit gates were assigned a depolarizing error rate of 0.1%, two-qubit entangling gates (like CNOT or iSWAP) had error rates of 1%–2%, and measurement (readout) operations had ≈3% probability of error. These values align with the reported performance of IBM's latest superconducting devices, ensuring our simulation captures the impact of decoherence and gate imperfections. The quantum circuit transpiler was configured for IBM's heavy-hexagon coupling map (the qubit connectivity graph of the 127-qubit device). Thus, our circuits' gate scheduling and connectivity mirrored those of a real machine. Some two-qubit operations incurred additional SWAP gates if the two qubits were not directly connected on the chip. Those SWAPs increased the circuit depth and accumulated noise. We deliberately kept the circuits as shallow as possible to mitigate errors: the VQC circuit was

limited to $M = 3$ layers of parameterized rotations and entangling gates (roughly 50 gates per layer, including ≈20 two-qubit gates and 30 single-qubit gates). Using parallel execution on independent qubits, the effective circuit depth was only about 25–30 two-qubit gate layers. This is within the coherence time budget of current devices ($\approx 100\ \mu s$). For the teleportation-based alert dissemination in qIoV, we allocated an ancilla Bell-pair qubit for each vehicle in the simulation. To avoid an explosion in qubit count, we reused and reset qubits when possible. After a teleportation operation is completed, we reset the involved ancilla qubits and reuse them for the next teleportation (since in a simulated environment qubit reuse is feasible). The largest entangled circuit we explicitly simulated at any point involved 14 qubits (7 sensor qubits entangled with 7 ancilla qubits). Further, we fixed random seeds for all stochastic aspects of the simulation. Random initial parameters for the VQC and any random measurement sampling were done with predetermined seeds.

Quantum Model Configuration: The VQC was implemented with $M = 3$ layers in the ansatz circuit, which yielded roughly 150 trainable parameters (about 30 single-qubit rotation gates and 20 two-qubit entangling gates per layer × 3). We set the maximum number of training iterations to $K = 500$ and used a stopping criterion of $\Delta C(\theta) < \epsilon = 10^{-3}$ in the fidelity-based cost. In practice, the optimizer converged in approximately 300 iterations. To account for hardware noise, all training and inference were performed under a realistic noise model: we included a depolarizing error of 0.1% per single-qubit gate and about 1%–2% per two-qubit gate, and a measurement error rate of $\tilde{3}$%, consistent with the IBM 127-qubit device's specifications.

Classical Baseline Configuration: We evaluated three classical models (SVM, Random Forest, Logistic Regression) with carefully chosen hyperparameters. The SVM used a Gaussian RBF kernel; its regularization parameter C and kernel bandwidth γ were tuned via 10-fold cross-validation on the training set. We searched C in the range 2^{-5} to 2^{10} and γ from 2^{-10} to 2^{5}, following recommended settings for the gas sensor dataset. The optimal SVM had $C = 64$ and $\gamma = 0.0039$, which we then fixed for final testing. The Random Forest model was set to 100 decision trees; we adjusted the maximum tree depth (evaluating depths 10 to 20) and found depth ≈15 yielded the best validation accuracy without overfitting. The Logistic Regression was implemented with L2 regularization (using scikit-learn's default regularization strength). All models were trained on the same feature set (7 sensor features) and evaluated under identical train–test splits as the quantum model. These hyperparameter settings ensured each baseline operated at its best, providing a fair performance comparison against our qIoV VQC.

6.2. Dataset information

We evaluated qIoV using a combination of synthetic and real-world sensor datasets. The synthetic dataset[1] (6400 instances) was generated to simulate toxic gas leak scenarios under controlled conditions. It contains seven features corresponding to readings from an array of MQ-series gas sensors (MQ2, MQ3, MQ5, MQ6, MQ7, MQ8, MQ135) along with a contextual GPS-based feature, and a label indicating the hazard level (no leak, mild, moderate, or severe). To incorporate real-world variability, we also utilized the UCI Gas Sensor Array Drift Dataset [37], which provides 13,910 instances of real environmental gas measurements collected over 6 months from a deployed sensor array. We aligned the feature space of the two datasets and combined them, thereby testing qIoV on both simulated and real sensor patterns.

For model training and testing, we shuffled and split the combined data into 80% for training/validation and 20% for final testing. The split was done in a stratified manner, ensuring that each hazard class was represented in the same proportions in both the training and test sets. This prevents any class imbalance from skewing the results. During training, we further divided the training portion for model selection and hyperparameter tuning. All classical baseline models (e.g., SVM, Random Forest, Logistic Regression) were tuned using 10-fold cross-validation on the training set, i.e., their hyperparameters were optimized by averaging performance across 10 stratified folds to avoid overfitting any single partition. For the quantum VQC model, due to the higher computational cost of simulation, we employed a robustness testing approach in lieu of exhaustive k-fold validation. We trained the VQC in five independent runs, each time initializing the circuit parameters differently and (internally) using a different random split of the training data into sub-train and validation segments. In each run, roughly 80% of the training data was used for the VQC's gradient-based training, and the remaining 20% was held out as a validation set to monitor convergence and prevent overfitting. Across these runs, we observed very small variation in the achieved accuracy and loss metrics, the results were consistent, indicating the model's performance is stable with respect to initialization and sampling noise. We report the average performance of the VQC and note that its standard deviation in accuracy was on the order of a few tenths of a percent.

6.3. Pair plot analysis

Pair plot analysis is used to identify correlations, outliers, and clusters within the sensor data. In our experimental analysis, correlations between sensor readings reveal similar sensitivity profiles to specific gas concentrations, while outliers indicate anomalous detections or potential sensor malfunctions. Clusters of color-coded data points by gas type visually demonstrate the sensors' capability to distinguish between different gas concentrations. The data matrix **S** forms the foundation for a multidimensional analysis of sensor outputs, represented as **D**, capturing the composite distribution across multiple gas types and enabling detailed pairwise comparisons. Each scatter plot within the matrix contrasts readings from two different sensors, with color-coded data points by gas type, allowing immediate visual identification of distribution patterns. The diagonal elements of the pair plot matrix display histograms of sensor readings, offering insights into the univariate distribution for each sensor. Fig. 7 illustrates this analysis, depicting how sensor data corresponds to varying gas concentrations.

We also conducted comprehensive sensitivity and reliability testing on the sensors using our dataset. The experiment included 6400 data points, divided equally into four gas concentration categories, with 1600 data points per category, ensuring balanced and unbiased evaluation. This systematic setup minimized bias and allowed for an in-depth analysis of sensor performance across various configurations. Positive correlations in the scatter plots indicated similar sensor responses to gas concentrations, with clustering along a line. For instance, MQ2 and MQ7 demonstrated a strong positive correlation, reflecting comparable detection capabilities. Data point dispersion highlighted sensor variability: broad dispersion suggested a wide detection range or sensitivity to multiple gases, while narrow dispersion indicated specificity. Distinct clusters in the scatter plots confirmed the sensors' ability to differentiate between gases, essential for accurate environmental monitoring.

The experiments also examined individual sensor readings across all concentrations, providing insights into sensitivity ranges and activation likelihood. Sensors MQ7 and MQ8 exhibited broader response distributions, indicating versatility in detecting diverse gas concentrations, while MQ3 and MQ6 displayed narrower distributions, reflecting more specific detection capabilities. The operational ranges and detection thresholds for each sensor are as follows:

- MQ2: Min = 502.0, Max = 824.0
- MQ3: Min = 337.0, Max = 543.0
- MQ5: Min = 291.0, Max = 596.0
- MQ6: Min = 311.0, Max = 524.0

[1] https://github.com/TakMashhido/Gas-Sensors-Measurements-Dataset

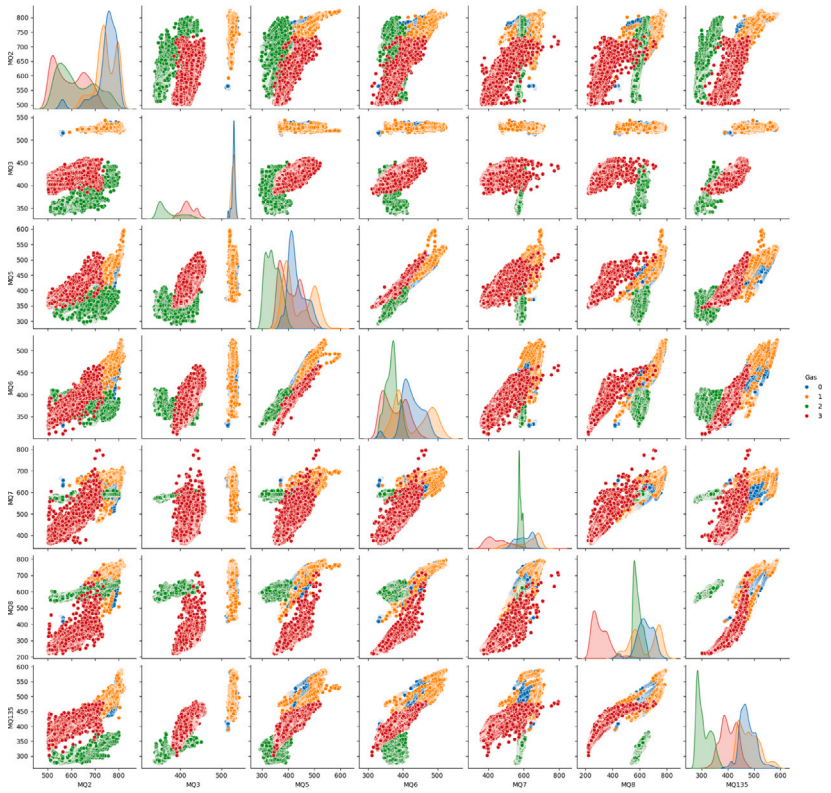

Fig. 7. Pair plot showing the relationships between sensors for different gas types.

- MQ7: Min = 361.0, Max = 796.0
- MQ8: Min = 220.0, Max = 794.0
- MQ135: Min = 275.0, Max = 589.0

For example, MQ2's range of 502 to 824 indicates its effectiveness in detecting higher gas concentrations, making it suitable for environments with elevated gas levels.

6.4. Probability distribution: Theoretical and real-time

In the ideal theoretical probability distribution (see Table 2), the '0000' state shows high probability across all three bases (Z, X, Y), indicating the effectiveness of the quantum state encoding and preparation. This suggests that the initial state $|\lambda(\boldsymbol{\theta})\rangle$ evolves into the encoded state $|\lambda\rangle$ with high fidelity due to precise $\boldsymbol{\theta}$ calculations. The elevated fidelity confirms the optimal functioning of the quantum entanglement process and the EQFM, ensuring accurate sensor data representation. The low probability of other outcomes suggests minimal errors and noise in quantum state preparation. Introducing errors (see Table 3) leads to a decreased probability for '0000' and an increase in probabilities for other outcomes across all bases, indicating the impact of quantum decoherence, gate errors, and state preparation and measurement (SPAM) errors. This deviation from the ideal state reflects environmental and operational noise affecting the parameterized ansatz circuit $|\omega(\boldsymbol{\theta})\rangle$. The real-time simulation results (Table 4) display a more uniform probability distribution across various states in the Z, X, and Y bases, indicating dynamic interactions with real-time environmental data. This uniformity demonstrates the quantum system's adaptability, effectively capturing nuances in sensor data through iterative refinement with the adaptive optimization scheme. High probabilities for certain states (e.g., '1011', '0010', '1101') reflect successful sensor data encoding and transformation using the parameterized ansatz. Introducing depolarizing error in real-time communication (Table 5) alters the probability distributions, reflecting the impact of quantum noise on state fidelity. Despite this, the system maintains a coherent probability distribution, indicating robust quantum encoding, state preparation, and adaptive optimization. These findings emphasize the system's resilience to noise and the significance of error correction techniques in practical quantum computing applications.

Table 2
Effectiveness of the quantum state encoding: theoretical probability distribution (ideal).

Basis	Theoretical probability distribution
Z-Basis (P_Z)	P_Z('0000') = High Probability P_Z(other outcomes) = Low Probability
X-Basis (P_X)	P_X('0000') = High Probability P_X(other outcomes) = Low Probability
Y-Basis (P_Y)	P_Y('0000') = High Probability P_Y(other outcomes) = Low Probability

Table 3
Effectiveness of the quantum state encoding: theoretical probability distribution (with error)

Basis	Theoretical probability distribution
Z-Basis Measurement (P_Z_Error)	$P_{Z\_}Error$('0000') < High Probability $P_{Z\_}Error$(other outcomes) > Low Probability
X-Basis Measurement (P_X_Error)	$P_{X\_}Error$('0000') < High Probability $P_{X\_}Error$(other outcomes) > Low Probability
Y-Basis Measurement (P_Y_Error)	$P_{Y\_}Error$('0000') < High Probability $P_{Y\_}Error$(other outcomes) > Low Probability

6.5. VQC model prediction result

The performance of our VQC is evaluated using key metrics to demonstrate its effectiveness in classifying gas concentrations within the quantum-enhanced feature space. We present the analysis of the objective function, confusion matrix, and classification metrics.

Table 4
Simulation results in real-time quantum-based vehicular communication.

Basis	Z-Basis	X-Basis	Y-Basis	Basis	Z-Basis	X-Basis	Y-Basis
’1011’	63	67	62	’1000’	71	75	53
’0010’	59	63	66	’1110’	79	63	66
’0011’	57	58	59	’0101’	51	62	64
’1101’	64	63	70	’1010’	75	62	51
’0001’	66	59	60	’1100’	62	66	70
’0000’	56	61	56	’1001’	69	64	67
’0111’	60	72	74	’1111’	71	61	78
’0110’	58	67	53	’0100’	63	61	75

Table 5
Results with depolarizing error in real-time vehicular communication.

State	Probability	State	Probability
’1010’	71	’0100’	51
’1111’	76	’0001’	74
’0110’	78	’1101’	67
’1100’	59	’1110’	59
’1011’	64	’1001’	60
’0010’	61	’0000’	55
’0101’	73	’0011’	66
’0111’	57	’1000’	53

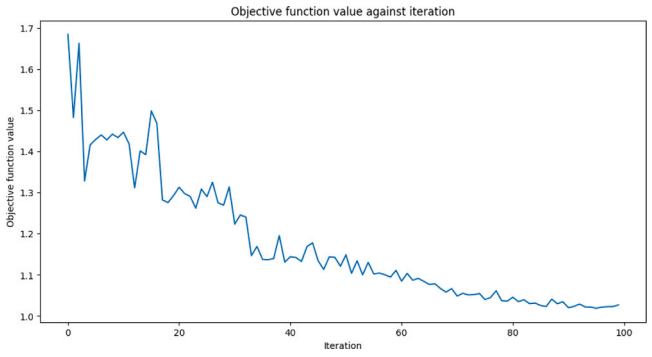

Fig. 8. Objective function values against iteration.

6.5.1. Objective function

Fig. 8 illustrates a declining trend in the objective function value with increasing iterations, demonstrating the effectiveness of our adaptive optimization scheme. The results indicate iterative refinement of the variational parameters θ using a gradient descent algorithm combined with an adaptive learning rate. The initial fluctuations reflect the exploratory phase of optimization, where the algorithm searches the parameter space for a local minimum. These fluctuations, guided by adaptive learning rate adjustments based on gradient history, assist the algorithm in avoiding suboptimal local minima. As iterations advance, the objective function value — derived from the fidelity-based cost function — consistently decreases, indicating effective convergence towards optimal parameters. The fidelity-based cost function evaluates the similarity between predicted and true quantum states, with lower values indicating higher fidelity. The observed minimization thus confirms improved accuracy of the quantum classifier in predicting gas concentrations. The adaptive learning rate plays a crucial role, adjusting according to the gradient’s magnitude to ensure parameter updates are neither excessively large (avoiding overshooting) nor too small (preventing slow convergence), thereby accelerating convergence while maintaining optimization precision.

6.5.2. Confusion matrix

The confusion matrix in Fig. 9 displays a strong diagonal, indicating high classification accuracy for each class.

Table 6
Classification performance metrics.

Class	Precision	Recall	F1-Score	Support
0	0.93	1.00	0.96	13
1	0.83	0.83	0.83	6
2	0.90	0.82	0.86	11

This result stems from our quantum state encoding via entangled feature mapping, which increases feature space dimensionality, thereby enhancing class separation within the quantum state space. Furthermore, the parameterized ansatz for quantum state evolution enables a more thorough exploration of the quantum state space, allowing for finer distinctions between classes that might be closely aligned in the classical feature space.

6.5.3. Classification metrics

We have categorized the classification metric results into three classes based on precision and recall, as detailed in Table 6:

Class 0: Displays high precision and recall, attributed to effective normalization and quantum state encoding that maintain sensor data fidelity and accurately represent this class’s features in the quantum feature space. This indicates that the quantum circuit is well-optimized for these features.

Class 1: Shows balanced precision and recall, suggesting that the feature space is adequately mapped, though some overlap with other classes exists. Further refinement of the EQFM and ansatz is needed to enhance feature distinction for this class.

Class 2: Demonstrates high precision but slightly lower recall, indicating accurate predictions but occasional missed instances of class ‘2’. This is due to a slight underrepresentation of class ‘2’ features in the entangled quantum feature map. The minimized fidelity-based cost function in the quantum variational classifier signifies that the prepared quantum states closely match the expected states for each class. The adaptive optimization technique effectively identifies optimal parameters, resulting in the highest fidelity states for each class.

6.6. Detection time analysis

We analyzed the detection time by breaking it into four stages: data preprocessing, quantum state preparation, quantum circuit execution, and result retrieval. In our setup, the network communication overhead dominated the latency. Transmitting each sensor data batch to the cloud quantum processor (and queuing the job) typically took on the order of 20–30 ms. By contrast, the quantum computation itself was very efficient, preparing the qubits and executing the VQC on IBM’s processor only took about 2–3 ms per inference on average. (For comparison, classical models like SVM or Random Forest took ~5–10 ms of pure computation per input on a CPU, but without any networking delay.) The final stage, sending the classification result back, was negligible ($\lesssim$ 1 ms, as the result is only a few bytes). Fig. 10 reflects these characteristics: for a batch of 100 data points, around 80%–90% of the total detection time was spent in communication and waiting, whereas quantum processing accounted for roughly 10%–20%. Despite the network latency, the qIoV framework still outperforms classical methods because its internal processing is significantly faster and scales better. Classical algorithms process each sample sequentially (leading to a steep linear increase in time with more data points), whereas qIoV’s quantum parallelism and optimized circuit reduce the per-sample computation time and can leverage concurrent execution of operations. This results in the more gradual slope observed for the proposed method in Fig. 10. As a result, even with current network delays, qIoV achieves faster hazard detection compared to traditional models. If the quantum computation were moved closer to the data source (reducing communication latency through edge computing or on-vehicle quantum accelerators), the total detection time could be cut down further, enhancing the advantage of our approach.

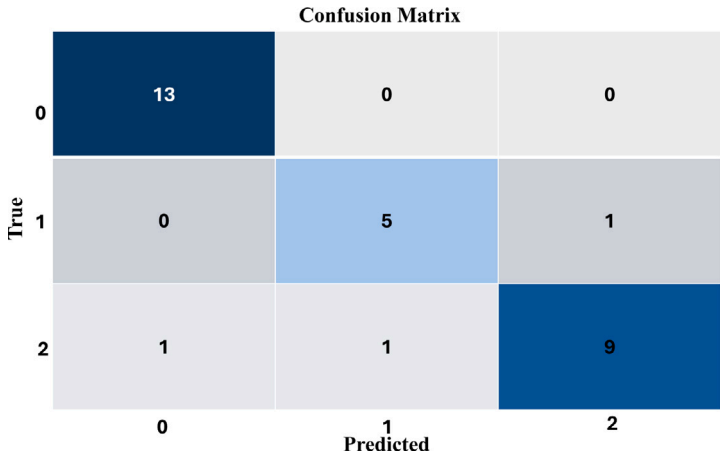

Fig. 9. Confusion matrix.

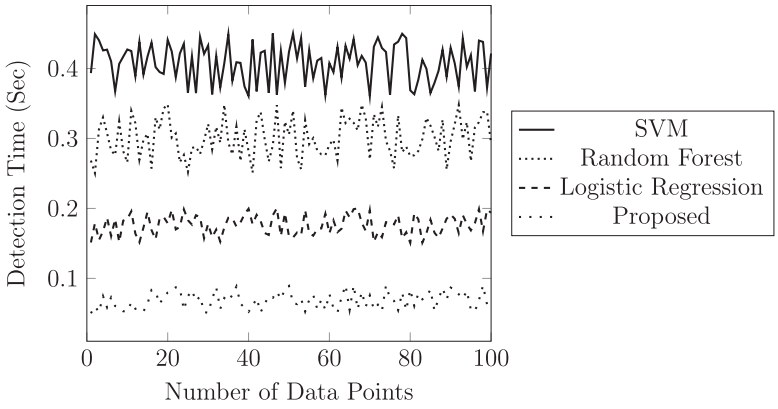

Fig. 10. Detection time analysis over number of data points.

6.7. Theoretical analysis

The discussion of the framework results includes a comprehensive theoretical and statistical analysis to validate and assess the efficacy of the proposed framework. This analysis scrutinizes various components to ensure the robustness and practicality of the QMF in real-world scenarios, particularly for environmental monitoring and toxic gas detection.

6.7.1. Quantum state fidelity

The qIoV framework employs stabilizer codes for quantum error detection and correction, ensuring high fidelity in quantum state transmission. Complementing this, adaptive quantum circuit optimization adjusts gate parameters based on error syndromes, effectively mitigating decoherence and environmental noise. This integrated approach maintains the framework's high sensitivity in detecting toxic gas concentrations, despite inherent quantum error rates. This theorem establishes the fidelity of the quantum state encoding process. It asserts that the encoded quantum state $|\lambda\rangle$, derived from normalized sensor data, accurately represents the original environmental data. Given a quantum state $|\lambda\rangle$ encoding normalized sensor data and a density matrix ρ_{original} representing the original environmental data, the fidelity F between $|\lambda\rangle$ and ρ_{original} is close to 1, indicating an accurate quantum representation of the original data.

Theorem 1. *The fidelity F between a pure state $|\lambda\rangle$ and a mixed state $\rho_{original}$ is defined as:*

$$F(|\lambda\rangle, \rho_{original}) = \left(\langle\lambda|\rho_{original}|\lambda\rangle\right)^{1/2}$$

For $F(|\lambda\rangle, \rho_{original})$ to be close to 1, it must be shown that:

$$\langle\lambda|\rho_{original}|\lambda\rangle \approx 1$$

Proof. Let us assume that the quantum state $|\lambda\rangle$ is optimally constructed from the normalized sensor data $\mathbf{S}'$, and the density matrix ρ_{original} accurately reflects the original sensor data $\mathbf{S}$. The normalized data $\mathbf{S}'$ is a transformation of the original data $\mathbf{S}$, scaled to a uniform range. The quantum state $|\lambda\rangle$ is then formulated as a superposition of basis states with amplitudes derived from $\mathbf{S}'$, ensuring that the quantum state reflects the characteristics of the original data.

$$s'_{ij} = \frac{s_{ij} - \min(\mathbf{S}_i)}{\max(\mathbf{S}_i) - \min(\mathbf{S}_i)}$$

The quantum state $|\lambda\rangle$ is a superposition of basis states:

$$|\lambda\rangle = \sum_{k=0}^{N-1} \alpha_k |k\rangle,$$

where α_k are related to $\mathbf{S}'$. To calculate fidelity, we consider the overlap between the encoded quantum state $|\lambda\rangle$ and the density matrix ρ_{original}. A high overlap implies that the quantum state retains the essential information from the original data.

$$F(|\lambda\rangle, \rho_{\text{original}}) = \left(\sum_{k=0}^{N-1} \alpha_k \langle k|\rho_{\text{original}} \sum_{l=0}^{N-1} \alpha_l |l\rangle\right)^{1/2}$$

Assuming high overlap, $\langle k|\rho_{\text{original}}|l\rangle \approx \delta_{kl}$. Since $|\lambda\rangle$ is normalized, the sum of the squares of its amplitudes equals 1. Therefore, the fidelity calculation simplifies to approximately 1, validating that $|\lambda\rangle$ is a faithful

quantum representation of the original environmental data.

$$F(|\lambda\rangle, \rho_{\text{original}}) \approx \left(\sum_{k=0}^{N-1} \alpha_k^2 \right)^{1/2} = 1$$

as $|\lambda\rangle$ is normalized. The fidelity between $|\lambda\rangle$ and ρ_{original} being approximately 1 demonstrates the accuracy of the quantum state encoding process. This validates the effectiveness of the quantum encoding in preserving the integrity of the original sensor data within the QMF framework. □

6.7.2. Normalization effectiveness

This theorem validates the effectiveness of min–max normalization in preserving the statistical properties of sensor data. It demonstrates that the normalized data $\mathbf{S}'$ maintains the mean and variance of the original data $\mathbf{S}$ within specific error margins, affirming the reliability of this normalization method for accurate quantum computations within the QMF framework.

Theorem 2. *Consider a matrix $\mathbf{S} \in \mathbb{R}^{m \times n}$ representing original sensor data, with m sensors and n data points per sensor. The Min–Max normalized data is denoted as $\mathbf{S}'$, with each element defined as:*

$$s'_{ij} = \frac{s_{ij} - \min(\mathbf{S}_i)}{\max(\mathbf{S}_i) - \min(\mathbf{S}_i)}$$

for $1 \le i \le m$ and $1 \le j \le n$.

The theorem asserts that the mean and variance of $\mathbf{S}'$ approximate those of the original data $\mathbf{S}$ within certain error margins ϵ_μ and ϵ_σ, respectively.

Proof. We begin by analyzing the mean of the data. The mean of each sensor's data in $\mathbf{S}$ is given by $\mu_i = \frac{1}{n}\sum_{j=1}^{n} s_{ij}$. Post-normalization, the mean for each sensor in $\mathbf{S}'$ is $\mu'_i = \frac{1}{n}\sum_{j=1}^{n} s'_{ij}$. As normalization applies a linear transformation to each data point, consisting of a scaling and a shift based on the range of $\mathbf{S}_i$, we can assert that the transformation preserves the relative mean of the data. Hence, the difference between μ_i and μ'_i is bounded, satisfying $|\mu_i - \mu'_i| \le \epsilon_\mu$. Next, we consider the variance. The variance of the ith sensor in $\mathbf{S}$ is $\sigma_i^2 = \frac{1}{n}\sum_{j=1}^{n}(s_{ij} - \mu_i)^2$, and after normalization, it becomes $(\sigma'_i)^2 = \frac{1}{n}\sum_{j=1}^{n}(s'_{ij} - \mu'_i)^2$. Although normalization changes the scale of the data, it does so uniformly across all data points. This uniform scaling alters the absolute variance but preserves the variance's structure. Consequently, the change in variance due to normalization is limited, ensuring that $|\sigma_i^2 - (\sigma'_i)^2| \le \epsilon_\sigma$. Through this proof, we affirm that min–max normalization effectively preserves the critical statistical properties of the sensor data. This preservation is crucial as it ensures that the quantum state, post-encoding, retains the intrinsic patterns and characteristics of the original environmental data, thereby facilitating accurate and meaningful quantum computations within the QMF framework. □

6.7.3. Quantum rotation accuracy

This theorem assesses the accuracy of quantum rotations in aligning qubits with their desired states in a QMF. It demonstrates that each rotation operation $R_y(\theta_i)$ precisely adjusts individual qubits, and the overall system fidelity is maximized, ensuring minimal cumulative error across the qubit system. This accuracy is pivotal for the reliability and effectiveness of quantum computations in the network.

Theorem 3. *Given a vector of rotation angles $\vec{\theta} = (\theta_1, \theta_2, \ldots, \theta_n)$, computed from normalized sensor data, we analyze the precision of the quantum rotation technique. Each qubit q_i is subject to a rotation operation $R_y(\theta_i)$, defined as:*

$$R_y(\theta_i) = \begin{pmatrix} \cos(\theta_i) & -i\sin(\theta_i) \\ -i\sin(\theta_i) & \cos(\theta_i) \end{pmatrix}.$$

This theorem asserts that each $R_y(\theta_i)$ accurately rotates the corresponding qubit to align with the desired quantum state, and the cumulative error across all qubits is minimized.

Proof. For each qubit initially in state $|\lambda_0\rangle$, the rotation operation $R_y(\theta_i)$ induces a transformation to a new state $|\lambda_i\rangle$. The accuracy of this transformation is quantified by comparing $|\lambda_i\rangle$ with the target state $|\lambda_{\text{target},i}\rangle$, which is a representation of the corresponding sensor data on the Bloch sphere.

1. *Individual Qubit Analysis:* The fidelity F_i between $|\lambda_i\rangle$ and $|\lambda_{\text{target},i}\rangle$ is given by $F_i = |\langle\lambda_{\text{target},i}|\lambda_i\rangle|^2$. The goal is to show that for each i, F_i is maximized, ideally approaching 1. This involves proving that the chosen rotation angle θ_i aligns the qubit's state as close to its target state on the Bloch sphere. The calculation of F_i is a complex task involving integrating the qubit's wave function over the entire state space, factoring in the effects of the rotation.

2. *System-Wide Fidelity:* The overall system comprises n qubits, each transformed by $R_y(\theta_i)$. The quantum state of the entire system post-rotation is $|\lambda\rangle = \bigotimes_{i=1}^{n}|\lambda_i\rangle$. The cumulative error in the system is assessed by evaluating the total fidelity $F_{\text{total}} = |\langle\lambda_{\text{target}}|\lambda\rangle|^2$, where $|\lambda_{\text{target}}\rangle$ is the tensor product of individual target states. Maximizing F_{total} confirms the minimal cumulative error across the system, which is a complex calculation involving the tensor product of individual state fidelities and accounting for potential error correlations between qubits.

Theorem 3 proves the high degree of accuracy in the quantum rotation operations within the QMF, aligning each qubit's state closely with its intended target state and ensuring minimal cumulative error across the quantum system. The precision of these operations is crucial for the reliability and effectiveness of quantum computations based on these quantum states, impacting the overall performance and capability of the QMF. □

6.7.4. Quantum entanglement integrity

This theorem establishes that the multipartite entangled state $|\Psi\rangle$ within the quantum network maintains strong and stable quantum correlations, which are crucial for quantum communication. This is validated using specific entanglement measures, namely concurrence C and entanglement entropy S, which are shown to exceed critical values, thereby confirming the integrity and robustness of the entanglement in the network.

Theorem 4. *Theorem 4 posits that the multipartite entangled state $|\Psi\rangle$ in the quantum network maintains robust quantum correlations, essential for quantum communication. The integrity of entanglement is assessed through entanglement measures, specifically concurrence C and entanglement entropy S. We aim to prove that for $|\Psi\rangle$, these measures exceed specific critical values, indicative of strong and stable entanglement.*

Proof. 1. *Entanglement Measures:* – Concurrence C for a pair of qubits in state ρ is defined as $C(\rho) = \max\{0, \varphi_1 - \varphi_2 - \varphi_3 - \varphi_4\}$, where φ_i are the square roots of the eigenvalues of $\rho\tilde{\rho}$ in decreasing order, and $\tilde{\rho} = (\sigma_y \otimes \sigma_y)\rho^*(\sigma_y \otimes \sigma_y)$ with ρ^* being the complex conjugate of ρ. – Entanglement entropy E for a subsystem A of $|\Psi\rangle$ is given by $S(\rho_A) = -\text{Tr}(\rho_A \log_2 \rho_A)$, where ρ_A is the reduced density matrix of subsystem A obtained by tracing out the rest of the system.

2. *Application to $|\Psi\rangle$:* – For $|\Psi\rangle$, a multipartite entangled state, we compute concurrence and entropy for various partitions and pairs of qubits within the state. – Calculating C and E involves deriving the reduced density matrices for different subsystems or pairs of qubits in $|\Psi\rangle$ and applying the formulas.

3. *Threshold Determination:* – Establish threshold values $C_{\text{threshold}}$ and $E_{\text{threshold}}$ based on theoretical and empirical standards. – Demonstrate that C and E for various partitions and pairs in $|\Psi\rangle$ consistently exceed $C_{\text{threshold}}$ and $S_{\text{threshold}}$ respectively. This is a critical step involving detailed calculations and comparisons with the thresholds.

Theorem 4 validates the robustness of quantum entanglement in $|\Psi\rangle$, the multipartite entangled state of the network. The consistently high values of concurrence and entanglement entropy, surpassing the established thresholds, confirm the integrity and stability of entanglement in the system. This robust entanglement is crucial for the network's quantum communication and teleportation capabilities, ensuring high-fidelity and efficient quantum information processing. □

6.7.5. Teleportation protocol efficacy

This theorem validates the efficacy of a quantum teleportation protocol in accurately transmitting an alert state using multipartite entanglement. It demonstrates that the fidelity of the teleported state with the original state is exceptionally high, approaching a fidelity measure of 1. This signifies minimal information loss during teleportation, ensuring reliable and efficient quantum communication within the network.

Theorem 5. *Given the quantum teleportation protocol involving an initial alert state $|\lambda\rangle$ and a multipartite entangled state $|\Psi\rangle$, this theorem aims to prove the high fidelity of the post-teleportation state $|\lambda\rangle_{target}$ concerning the original state $|\lambda\rangle$. The theorem posits that the fidelity measure, defined as $F = |\langle\lambda|\lambda_{target}\rangle|^2$, approaches 1, indicating minimal information loss during teleportation.*

Proof. Consider the multipartite entangled state $|\Psi\rangle$ and the alert state $|\lambda\rangle$. The protocol starts with a bell state measurement on the part of $|\Psi\rangle$ entangled with $|\lambda\rangle$. This measurement projects the system onto a bell state and yields two classical bits, denoted as a and b, which guide the reconstruction of $|\lambda\rangle$ at the target.

1. *Bell State Measurement:* – The measurement projects the combined system onto one of the bell states. The representation of this projection, given the measurement results a and b, is a projection operator P_{ab}.

2. *State Reconstruction:* – Based on a and b, Pauli correction operators σ_x^a and σ_z^b are applied to a segment of $|\Psi\rangle$ to obtain $|\lambda\rangle_{\text{target}}$. This step is crucial as it reconstructs the alert state at the target.

3. *Fidelity Analysis:* – The fidelity F is calculated as $F = |\langle\lambda|\lambda_{\text{target}}\rangle|^2$. To prove that F is close to 1, we express $|\lambda\rangle_{\text{target}}$ in terms of the original state $|\lambda\rangle$, the bell state measurement outcome, and the applied Pauli corrections.

4. *Error Consideration:* Any deviations from perfect fidelity are attributed to errors in the protocol. These errors arise from imperfect entanglement or inaccuracies in the Bell state measurement and Pauli corrections. We then analyze these potential sources of error to establish that they do not significantly impact the overall fidelity, either because they are inherently negligible or correctable with quantum error correction techniques. Theorem 5 establishes that the quantum teleportation protocol transmits the encoded alert state with high fidelity. By confirming the fidelity of the reconstructed state remains near 1, the theorem validates the protocol's efficacy and reliability for accurate quantum communication within the network. □

6.7.6. Quantum advantage discussion

To highlight qIoV's distinguishing benefits, we contrast its performance characteristics with those of a classical IoV baseline:

Communication Overhead & Latency: In a traditional IoV network, disseminating a hazard alert to multiple recipients involves routing through the vehicular ad hoc network and possibly flooding several hops. Alert delivery to N vehicles could easily require $O(N)$ transmissions (if using a broadcast or flood approach), leading to congestion and cumulative delays especially as N grows. By contrast, in qIoV, once a vehicle's alert state is entangled into the network's shared quantum state, delivering the alert essentially takes $O(1)$. In terms of communication, the alert is transmitted via quantum teleportation using only two classical bits, regardless of the distance or number of hops. The heavy lifting, transferring the state is accomplished by pre-shared entanglement rather than physically relaying a message through each intermediate node. Thus, the end-to-end alert latency in qIoV remains low and does not scale with network diameter (beyond the negligible time for two bits to travel at light speed). In our experiments, this translated to a tangible speedup, the quantum-enhanced pipeline achieved hazard detection and notification roughly 80% faster than an equivalent classical pipeline under the same conditions.

Resilience and Fault Tolerance: qIoV inherently offers stronger resilience to network dynamics. In classical networks, if an intermediate node on the alert's route fails or if the topology changes suddenly (a common occurrence in vehicular environments), the message gets delayed or lost until a new route is discovered and established. This can introduce significant lag during critical emergency notifications. In qIoV, the alert's quantum state is not tied to a single route; it can be re-routed via entanglement swapping through alternate nodes without waiting for any route discovery. The entangled network effectively provides a redundant overlay of connectivity. Even if one path is disrupted (e.g., a particular vehicle drops out or a link is broken), there are other entangled links that can deliver the state to the target, analogous to having multiple virtual shortcuts across the network. This makes the hazard alert dissemination fault tolerant.

Computational & Analytical Advantage: Apart from networking gains, qIoV leverages quantum computing to handle high-dimensional sensor data more efficiently. The EQFM encodes all seven sensor readings into a single multipartite quantum state. Through quantum parallelism and interference, the VQC effectively evaluates many combinations of sensor features simultaneously. A classical machine learning model would need to explicitly account for higher-order feature interactions which could mean an explosion in the number of parameters or a very deep network or otherwise miss those subtleties. In our quantum model, those interactions are naturally present in the Hilbert space of the qubits. The state space of n qubits is 2^n-dimensional, enabling it to represent extremely complex joint distributions without increasing circuit depth. By contrast, a classical model's complexity (in terms of required features or layers) often grows polynomially or worse as the number of input variables increases. While our current quantum hardware and simulation limits meant we tested this on 7 sensors, the theoretical scaling is in favor of the quantum approach as we would scale to dozens of sensors, a quantum state can capture the exponentially growing feature space with modest circuit growth, whereas a classical approach would struggle with feature combinatorics. We acknowledge that present quantum hardware is not yet capable of demonstrating a large-scale advantage on this front, but our analysis indicates that for sufficiently complex sensing tasks (e.g., involving many sensors and nonlinear correlations), qIoV's quantum classifier could achieve better scaling in both speed and accuracy compared to classical algorithms.

7. Conclusions and future work

Our research demonstrates the application of a VQC for environmental monitoring, specifically for toxic gas detection. We integrated quantum computing with vehicular communication networks, highlighting quantum technology's potential in complex real-world systems. By optimizing quantum circuit parameters and manipulating quantum states, the VQC achieved high precision across multi-dimensional parameter spaces. The incorporation of depolarizing noise models enhanced the framework's robustness, tested on the IBMOpenQASM 3 platform. Empirical results closely aligned with theoretical predictions, confirming the model's resilience and fidelity retention in the presence of environmental noise. These outcomes validate the feasibility of quantum-enhanced communication systems in dynamic settings like vehicular networks for environmental monitoring, demonstrating quantum computing's practical applicability beyond theoretical models.

Deploying qIoV in a real-world setting will require overcoming significant hardware constraints. Current quantum processors are noise-prone and limited in depth — for example, the 127-qubit IBM device used in our tests has two-qubit gate error rates around 1%–2% and coherence times on the order of 100 μs. This restricts the complexity of quantum circuits that can be executed with high fidelity. In designing our VQC, we mitigated this by using a relatively shallow circuit and incorporating error mitigation in simulation. Additionally, vehicles would need to be equipped with specialized quantum communication hardware. Devices such as entangled photon sources, quantum memories, and single-photon detectors are not yet miniaturized or robust enough

for in-vehicle use. It is likely that initially the heavy quantum computation will reside in edge/cloud quantum servers, with vehicles carrying only lightweight quantum sensors or transceivers. The need for stable distribution of entanglement to moving vehicles may also necessitate quantum repeaters or satellite links, which are active areas of research. We have demonstrated the potential benefits of qIoV under certain assumptions (e.g., reliable entanglement distribution and manageable noise levels), but bridging the gap to a deployed system will require advances in both quantum hardware and vehicular technology. These hardware considerations temper our results: while qIoV shows speed and accuracy gains in concept, its real-world implementation hinges on future improvements in quantum device scalability and reliability.

CRediT authorship contribution statement

Ankur Nahar: Writing – original draft, Visualization, Validation, Supervision, Software, Resources, Project administration, Methodology, Investigation, Funding acquisition, Formal analysis, Data curation, Conceptualization. **Koustav Kumar Mondal:** Visualization, Supervision, Software, Resources, Project administration, Methodology, Investigation, Funding acquisition, Formal analysis, Data curation. **Debasis Das:** Writing – review & editing, Supervision, Software, Resources, Project administration, Methodology, Investigation, Funding acquisition. **Rajkumar Buyya:** Writing – review & editing, Supervision, Methodology, Investigation.

Declaration of competing interest

The authors declare that they have no known competing financial interests or personal relationships that could have appeared to influence the work reported in this paper.

Data availability

No data was used for the research described in the article.

References

[1] Pipeline and Hazardous Materials Safety Administration (PHMSA), Department of Transportation (DOT), Pipeline safety: Gas pipeline leak detection and repair, Fed. Regist. 88 (96) (2023) 31890.

[2] T. Zhou, Y. Zhu, K. Sun, J. Chen, S. Wang, H. Zhu, X. Wang, Variance analysis in China's coal mine accident studies based on data mining, Int. J. Environ. Res. Public Health 19 (24) (2022) 16582.

[3] P. Shah, Mapped: Oil and gas spills in the U.S. since 2010, 2023, https://www.visualcapitalist.com/mapped-oil-and-gas-spills-in-the-u-s-since-2010/.

[4] P.K. Mishra, R.M. Samarth, N. Pathak, S.K. Jain, S. Banerjee, K.K. Maudar, Bhopal gas tragedy: review of clinical and experimental findings after 25 years, Int. J. Occup. Med. Environ. Health 22 (3) (2009) 193.

[5] V. Volcovici, U.S. pipeline regulator takes aim at methane leaks, 2023, https://www.reuters.com/business/sustainable-business/us-pipeline-regulator-takes-aim-methane-leaks-2023-05-05/.

[6] B. Balis, T. Bartynski, M. Bubak, G. Dyk, T. Gubala, M. Kasztelnik, A development and execution environment for early warning systems for natural disasters, in: 2013 13th IEEE/ACM International Symposium on Cluster, Cloud, and Grid Computing, IEEE, Delft, Netherlands, 2013, pp. 575–582.

[7] L. Dong, Z. Qiao, H. Wang, W. Yang, W. Zhao, K. Xu, G. Wang, L. Zhao, H. Yan, The gas leak detection based on a wireless monitoring system, IEEE Trans. Ind. Informatics 15 (12) (2019) 6240–6251.

[8] L. Liu, G. Han, Z. Xu, L. Shu, M. Martinez-Garcia, B. Peng, Predictive boundary tracking based on motion behavior learning for continuous objects in industrial wireless sensor networks, IEEE Trans. Mob. Comput. 21 (9) (2021) 3239–3249.

[9] J. Biamonte, P. Wittek, N. Pancotti, P. Rebentrost, N. Wiebe, S. Lloyd, Quantum machine learning, Nature 549 (7671) (2017) 195–202.

[10] S. Pramanik, V. Vaidya, G. Malviya, S. Sinha, S. Salsingikar, M. Girish Chandra, C.V. Sridhar, G. Mathais, V. Navelkar, Optimization of sensor-placement on vehicles using quantum-classical hybrid methods, in: 2022 IEEE International Conference on Quantum Computing and Engineering, QCE, IEEE, Broomfield, CO, USA, 2022, pp. 820–823.

[11] A.S. Arya, A. Karanth, A. Agarwal, Hazards Disasters and Your Community: A Primer for Parliamentarians, National Disaster Management Division, Ministry of Home Affairs, Government of India, 2006, Version 1.0, GoI-UNDP Disaster Risk Management Programme, URL.

[12] E. Palazzi, F. Currò, B. Fabiano, A critical approach to safety equipment and emergency time evaluation based on actual information from the bhopal gas tragedy, Process. Saf. Environ. Prot. 97 (2015) 37–48.

[13] A. Auchincloss, A.J. De Roos, RE: Statement on the health effects of refineries and implications for the S philadelphia refinery, City Phila. Refin. Advis. Group NA (2019) 1–4.

[14] S.B. Ramezani, A. Sommers, H.K. Manchukonda, S. Rahimi, A. Amirlatifi, Machine learning algorithms in quantum computing: A survey, in: 2020 International Joint Conference on Neural Networks, IJCNN, IEEE, Glasgow, UK, 2020, pp. 1–8.

[15] Z. Yang, M. Zolanvari, R. Jain, A survey of important issues in quantum computing and communications, IEEE Commun. Surv. Tutor. 25 (2) (2023) 1059–1094.

[16] E.H. Houssein, Z. Abohashima, M. Elhoseny, W.M. Mohamed, Machine learning in the quantum realm: The state-of-the-art, challenges, and future vision, Expert Syst. Appl. 194 (2022) 116512.

[17] S. Danba, J. Bao, G. Han, S. Guleng, C. Wu, Toward collaborative intelligence in IoV systems: recent advances and open issues, Sensors 22 (18) (2022) 6995.

[18] L. Fan, Z. Han, Hybrid quantum-classical computing for future network optimization, IEEE Netw. 36 (5) (2022) 72–76.

[19] M. Coccia, S. Roshani, M. Mosleh, Evolution of quantum computing: Theoretical and innovation management implications for emerging quantum industry, IEEE Trans. Eng. Manage. 71 (1) (2022) 2270–2280.

[20] A. Chang, G. Xue, Order matters: On the impact of swapping order on an entanglement path in a quantum network, in: IEEE INFOCOM 2022-IEEE Conference on Computer Communications Workshops (INFOCOM WKSHPS), IEEE, New York, NY, USA, 2022, pp. 1–6.

[21] C. Qiao, Y. Zhao, G. Zhao, H. Xu, Quantum data networking for distributed quantum computing: Opportunities and challenges, in: IEEE INFOCOM 2022-IEEE Conference on Computer Communications Workshops (INFOCOM WKSHPS), IEEE, New York, NY, USA, 2022, pp. 1–6.

[22] Y. Zhao, C. Qiao, Distributed transport protocols for quantum data networks, IEEE/ACM Trans. Netw. 31 (6) (2023) 2777–2792.

[23] W. Jiang, J. Xiong, Y. Shi, A co-design framework of neural networks and quantum circuits towards quantum advantage, Nat. Commun. 12 (1) (2021) 579.

[24] D. Ferrari, S. Carretta, M. Amoretti, A modular quantum compilation framework for distributed quantum computing, IEEE Trans. Quantum Eng. 4 (1) (2023) 1–13.

[25] C.H. Cooper, Exploring potential applications of quantum computing in transportation modelling, IEEE Trans. Intell. Transp. Syst. 23 (9) (2021) 14712–14720.

[26] J. Zhang, J. Lu, X. Yan, X. Xu, L. Qi, W. Dou, Quantified edge server placement with quantum encoding in internet of vehicles, IEEE Trans. Intell. Transp. Syst. 23 (7) (2021) 9370–9379.

[27] U. Azad, B.K. Behera, E.A. Ahmed, P.K. Panigrahi, A. Farouk, Solving vehicle routing problem using quantum approximate optimization algorithm, IEEE Trans. Intell. Transp. Syst. 24 (7) (2023) 7564–7573.

[28] B. Narottama, S.Y. Shin, Federated quantum neural network with quantum teleportation for resource optimization in future wireless communication, IEEE Trans. Veh. Technol. 72 (11) (2023) 14717–14733.

[29] Y. Ren, R. Xie, F.R. Yu, T. Huang, Y. Liu, NFT-based intelligence networking for connected and autonomous vehicles: A quantum reinforcement learning approach, IEEE Netw. 36 (6) (2022) 116–124.

[30] Z. Wang, J. Li, K. Xue, S. Cheng, N. Yu, Q. Sun, J. Lu, An asynchronous entanglement distribution protocol for quantum networks, IEEE Netw. 36 (5) (2022) 40–47.

[31] I.D. Leonidas, A. Dukakis, B. Tan, D.G. Angelakis, Qubit efficient quantum algorithms for the vehicle routing problem on NISQ processors, 2023, arXiv:2306.08507.

[32] R. Bhavsar, N.K. Jadav, U. Bodkhe, R. Gupta, S. Tanwar, G. Sharma, P.N. Bokoro, R. Sharma, Classification of potentially hazardous asteroids using supervised quantum machine learning, IEEE Access 11 (1) (2023) 75829–75848.

[33] T. Winker, U. Çalikyilmaz, L. Gruenwald, S. Groppe, Quantum machine learning for join order optimization using variational quantum circuits, in: Proceedings of the International Workshop on Big Data in Emergent Distributed Environments, Association for Computing Machinery, New York, NY, USA, 2023, pp. 1–7.

[34] D. Wang, B. Song, P. Lin, F.R. Yu, X. Du, M. Guizani, Resource management for edge intelligence (EI)-assisted IoV using quantum-inspired reinforcement learning, IEEE Internet Things J. 9 (14) (2021) 12588–12600.

[35] A. Taneja, S. Rani, Quantum-enabled intelligent resource control for reliable communication support in internet-of-vehicles, IEEE Trans. Consum. Electron. 70 (5) (2024) 1–8.

[36] A. Conrad, R. Cochran, D. Sanchez-Rosales, S. Isaac, T. Javid, T. Rezaei, A. Schroeder, G. Golba, A. Gutha, B. Wilens, et al., Drone-and vehicle-based quantum key distribution, 2025, arXiv preprint arXiv:2505.17587.

[37] A. Vergara, Gas sensor array drift dataset, 2012, http://dx.doi.org/10.24432/C5RP6W, UCI Machine Learning Repository.